

Table 2. Cont.

| | | |
|--------------------------|-----------------------------|------------------------|
| Cytosine | ↑ by 5/6Nx, ↓ by AST-120 | ↑ in CKD patients |
| 5-Methylcytosine | ↑ by 5/6Nx, ↓ by AST-120 | Not Detected |
| Imidazole-4-acetate | ↑ by 5/6Nx, ↓ by AST-120 | Not Detected |
| Anthranilate | N.S. by 5/6Nx, ↓ by AST-120 | Not Detected |
| Glycerophosphorylcholine | N.S. by 5/6Nx, ↓ by AST-120 | N.S. |
| Nicotinamide | N.S. by 5/6Nx, ↓ by AST-120 | Not Detected |
| Gln | N.S. by 5/6Nx, ↓ by AST-120 | ↓ in CKD patients |
| Asn | N.S. by 5/6Nx, ↓ by AST-120 | ↑ in CKD patients |
| Dihydroraçil | N.S. by 5/6Nx, ↓ by AST-120 | Not Detected |
| Glu | N.S. by 5/6Nx, ↓ by AST-120 | N.S. |
| Creatine | N.S. by 5/6Nx, ↓ by AST-120 | N.S. |
| g-Butyrobetaine | N.S. by 5/6Nx, ↓ by AST-120 | ↑ in CKD patients |
| 1-Methylnicotinamide | N.S. by 5/6Nx, ↓ by AST-120 | N.S. |
| Itp | ↓ by 5/6Nx, ↑ by AST-120 | ↓ in CKD patients [24] |
| Trimethylamine N-oxide | N.S. by 5/6Nx, ↑ by AST-120 | ↑ in CKD patients [25] |
| | | ↑ in uremia [19] |

5. Conclusion

We newly identified 4 anions and 19 cations whose plasma levels are changed by AST-120 treatment in 5/6Nx rats. This study provides useful information, not only for identifying the indicators of AST-120, but also for clarifying changes in the metabolic profile by AST-120 treatment in the clinical setting.

Conflict of Interest

The authors declare no conflict of interest.

References

- Levey, A.S.; Coresh, J. Chronic kidney disease. *Lancet* **2012**, *379*, 165–180.
- Go, A.S.; Chertow, G.M.; Fan, D.; McCulloch, C.E.; Hsu, C.Y. Chronic kidney disease and the risks of death, cardiovascular events, and hospitalization. *N. Engl. J. Med.* **2004**, *351*, 1296–1305.
- Watanabe, H.; Miyamoto, Y.; Otagiri, M.; Maruyama, T. Update on the pharmacokinetics and redox properties of protein-bound uremic toxins. *J. Pharm. Sci.* **2011**, *100*, 3682–3695.
- Vanholder, R.; Glorieux, G.; De Smet, R.; Lameire, N. New insights in uremic toxins. *Kidney Int.* **2003**, *63* (Suppl. 84), S6–S10.
- Vanholder, R.; Baurmeister, U.; Brunet, P.; Cohen, G.; Glorieux, G.; Jankowski, J. A bench to bedside view of uremic toxins. *J. Am. Soc. Nephrol.* **2008**, *19*, 863–870.
- Niwa, T. Role of indoxyl sulfate in the progression of chronic kidney disease and cardiovascular disease: Experimental and clinical effects of oral sorbent AST-120. *Ther. Apher. Dial.* **2011**, *15*, 120–124.
- Goto, S.; Yoshiya, K.; Kita, T.; Fujii, H.; Fukagawa, M. Uremic toxins and oral adsorbents. *Ther. Apher. Dial.* **2011**, *15*, 132–134.
- Niwa, T.; Miyazaki, T.; Hashimoto, N.; Hayashi, H.; Ise, M.; Uehara, Y.; Maeda, K. Suppressed serum and urine levels of indoxyl sulfate by oral sorbent in experimental uremic rats. *Am. J. Nephrol.* **1992**, *12*, 201–206.
- Kikuchi, K.; Itoh, Y.; Tateoka, R.; Ezawa, A.; Murakami, K.; Niwa, T. Metabolomic search for uremic toxins as indicators of the effect of an oral sorbent AST-120 by liquid chromatography/tandem mass spectrometry. *J. Chromatogr. B* **2010**, *878*, 2997–3002.
- Ueda, S.; Yamagishi, S.; Takeuchi, M.; Kohno, K.; Shibata, R.; Matsumoto, Y.; Kaneyuki, U.; Fujimura, T.; Hayashida, A.; Okuda, S. Oral adsorbent AST-120 decreases serum levels of AGEs in patients with chronic renal failure. *Mol. Med.* **2006**, *12*, 180–184.
- Toyohara, T.; Suzuki, T.; Morimoto, R.; Akiyama, Y.; Souma, T.; Shiwaku, H.O.; Takeuchi, Y.; Mishima, E.; Abe, M.; Tanemoto, M.; *et al.* SLCO4C1 transporter eliminates uremic toxins and attenuates hypertension and renal inflammation. *J. Am. Soc. Nephrol.* **2009**, *20*, 2546–2555.
- Toyohara, T.; Suzuki, T.; Akiyama, Y.; Yoshihara, D.; Takeuchi, Y.; Mishima, E.; Kikuchi, K.; Suzuki, C.; Tanemoto, M.; Ito, S.; *et al.* Metabolomic profiling of the autosomal dominant polycystic kidney disease rat model. *Clin. Exp. Nephrol.* **2011**, *15*, 676–687.

13. Toyohara, T.; Akiyama, Y.; Suzuki, T.; Takeuchi, Y.; Mishima, E.; Tanemoto, M.; Momose, A.; Toki, N.; Sato, H.; Nakayama, M.; *et al.* Metabolomic profiling of uremic solutes in CKD patients. *Hypertens. Res.* **2010**, *33*, 944–952.
14. Soga, T.; Ohashi, Y.; Ueno, Y.; Naraoka, H.; Tomita, M.; Nishioka, T. Quantitative metabolome analysis using capillary electrophoresis mass spectrometry. *J. Proteome Res.* **2003**, *2*, 488–494.
15. Soga, T.; Heiger, D.N. Amino acid analysis by capillary electrophoresis electrospray ionization mass spectrometry. *Anal. Chem.* **2000**, *72*, 1236–1241.
16. Soga, T.; Igarashi, K.; Ito, C.; Mizobuchi, K.; Zimmermann, H.P.; Tomita, M. Metabolomic profiling of anionic metabolites by capillary electrophoresis mass spectrometry. *Anal. Chem.* **2009**, *81*, 6165–6174.
17. Soga, T.; Ueno, Y.; Naraoka, H.; Ohashi, Y.; Tomita, M.; Nishioka, T. Simultaneous determination of anionic intermediates for *Bacillus subtilis* metabolic pathways by capillary electrophoresis electrospray ionization mass spectrometry. *Anal. Chem.* **2002**, *74*, 2233–2239.
18. Soga, T.; Baran, R.; Suematsu, M.; Ueno, Y.; Ikeda, S.; Sakurakawa, T.; Kakazu, Y.; Ishikawa, T.; Robert, M.; Nishioka, T.; Tomita, M. Differential metabolomics reveals ophthalmic acid as an oxidative stress biomarker indicating hepatic glutathione consumption. *J. Biol. Chem.* **2006**, *281*, 16768–16776.
19. Vanholder, R.; Van Laecke, S.; Glorieux, G. What is new in uremic toxicity? *Pediatr. Nephrol.* **2008**, *23*, 1211–1221.
20. Kand'ar, R.; Zakova, P. Allantoin as a marker of oxidative stress in human erythrocytes. *Clin. Chem. Lab. Med.* **2008**, *46*, 1270–1274.
21. Biedron, R.; Ciszek, M.; Tokarczyk, M.; Bobek, M.; Kurnyta, M.; Slominska, E.M.; Smolenski, R.T.; Marcinkiewicz, J. 1-Methylnicotinamide and nicotinamide: Two related anti-inflammatory agents that differentially affect the functions of activated macrophages. *Arch. Immunol. Ther. Exp. (Warsz.)* **2008**, *56*, 127–134.
22. Chlopicki, S.; Swies, J.; Mogielnicki, A.; Buczek, W.; Bartus, M.; Lomnicka, M.; Adamus, J.; Gebicki, J. 1-Methylnicotinamide (MNA), a primary metabolite of nicotinamide, exerts anti-thrombotic activity mediated by a cyclooxygenase-2/prostacyclin pathway. *Br. J. Pharmacol.* **2007**, *152*, 230–239.
23. Watala, C.; Kazmierczak, P.; Dobaczewski, M.; Przygodzki, T.; Bartus, M.; Lomnicka, M.; Slominska, E.M.; Durackova, Z.; Chlopicki, S. Anti-diabetic effects of 1-methylnicotinamide (MNA) in streptozocin-induced diabetes in rats. *Pharmacol. Rep.* **2009**, *61*, 86–98.
24. Swendseid, M.E.; Wang, M.; Vyhmeister, I.; Chan, W.; Siassi, F.; Tam, C.F.; Kopple, J.D. Amino acid metabolism in the chronically uremic rat. *Clin. Nephrol.* **1975**, *3*, 240–246.
25. Bain, M.A.; Faull, R.; Fornasini, G.; Milne, R.W.; Evans, A.M. Accumulation of trimethylamine and trimethylamine-N-oxide in end-stage renal disease patients undergoing haemodialysis. *Nephrol. Dial. Transplant.* **2006**, *21*, 1300–1304.

26. Wang, Z.; Klipfell, E.; Bennett, B.J.; Koeth, R.; Levison, B.S.; Dugar, B.; Feldstein, A.E.; Britt, E.B.; Fu, X.; Chung, Y.M.; *et al.* Gut flora metabolism of phosphatidylcholine promotes cardiovascular disease. *Nature* **2011**, *472*, 57–63.

© 2012 by the authors; licensee MDPI, Basel, Switzerland. This article is an open access article distributed under the terms and conditions of the Creative Commons Attribution license (<http://creativecommons.org/licenses/by/3.0/>).

Cyclin D2 in the basal process of neural progenitors is linked to non-equivalent cell fates

Yuji Tsunekawa¹, Joanne M Britto², Masanori Takahashi¹, Franck Polleux³, Seong-Seng Tan² and Noriko Osumi^{1,*}

¹Division of Developmental Neuroscience, United Core Centers for Advanced Research and Translational Medicine, Tohoku University Graduate School of Medicine, Sendai, Japan, ²Brain Development and Regeneration Laboratory, Florey Neuroscience Institutes, University of Melbourne, Melbourne, Victoria, Australia and ³Department of Cell Biology, Dorris Neuroscience Center, The Scripps Research Institute, La Jolla, CA, USA

Asymmetric cell division plays an indispensable role during corticogenesis for producing new neurons while maintaining a self-renewing pool of apical progenitors. The cellular and molecular determinants favouring asymmetric division are not completely understood. Here, we identify a novel mechanism for generating cellular asymmetry through the active transportation and local translation of *Cyclin D2* mRNA in the basal process. This process is regulated by a unique *cis*-regulatory sequence found in the 3' untranslated region (3'UTR) of the mRNA. Unequal inheritance of *Cyclin D2* protein to the basally positioned daughter cell with the basal process confers renewal of the apical progenitor after asymmetric division. Conversely, depletion of *Cyclin D2* in the apically positioned daughter cell results in terminal neuronal differentiation. We demonstrate that *Cyclin D2* is also expressed in the developing human cortex within similar domains, thus indicating that its role as a fate determinant is ancient and conserved.

The EMBO Journal advance online publication, 6 March 2012; doi:10.1038/emboj.2012.43

Subject Categories: cell & tissue architecture; neuroscience
Keywords: asymmetric cell division; corticogenesis; *Cyclin D2*; mRNA subcellular localization; neuronal differentiation

Introduction

During cortical development in mammals, the expansion of the cortical wall relies on large numbers of neurons to be generated by proliferating neuroepithelial cells (Smart, 1973). At early stages of corticogenesis (embryonic day 10.5 (E10.5)), these neuroepithelial cells divide symmetrically to yield more progenitors, resulting in a thickened pseudostratified sheet where the mitotic cells are concentrated mainly on the apical side of the epithelium (Rakic, 1988). The

dividing cells attached to the apical membrane are called apical progenitors (APs), and during the proliferative stage they undergo mostly symmetric cell divisions, producing daughter cells with equal fates (as neurons or more progenitors) (Huttner and Kosodo, 2005). Later in corticogenesis (E12.5–15.5), neuroepithelial cells become radial glia and start to divide asymmetrically, producing an AP with self-renewing capacity together with a terminally differentiated neuron or intermediate progenitor (IP) (Gotz and Huttner, 2005). Newly produced neurons migrate out of the ventricular zone (VZ) to form the cortical plate (CP), while intermediate progenitors divide symmetrically in the subventricular zone (SVZ) and generate more IPs or neurons (Haubensack *et al.*, 2004; Miyata *et al.*, 2004; Noctor *et al.*, 2004). APs undergoing symmetric and asymmetric divisions often overlap and coexist in the germinal zones (Huttner and Kosodo, 2005), but what is unclear is the motivation driving symmetric versus asymmetric divisions (Gotz and Huttner, 2005).

Asymmetric cell division of neural progenitor cells is critical for establishing the architectures of the mammalian cerebral cortex by regulating the balance between proliferative and neurogenic populations. This is achieved by producing daughter cells that are self-renewing together with daughter cells that become postmitotic neurons and thereby increasing the number of neurons while maintaining the number of APs (Gotz and Huttner, 2005; Kriegstein *et al.*, 2006). In addition, asymmetric cell division is capable of generating a third class of offspring known as the intermediate progenitor whose cell body lies in the SVZ and retracts its apical attachment prior to mitosis (Miyata *et al.*, 2004; Attardo *et al.*, 2008). These observations invite the question—what cellular factors influence mitotic descendants to become a self-renewing AP or a differentiated neuron?

A key issue in this debate concerns the roles played by structural elements such as the apical membrane or basal process, and their cytoplasmic constituents, in conferring AP fate. The cleavage plane *per se* is not an indicator of symmetric or asymmetric division (Kosodo *et al.*, 2004), but experimental randomization of the cleavage plane (by changing mitotic spindle orientation) decreases the number of APs (Konno *et al.*, 2008). Leaving cleavage plane aside, it has been suggested that asymmetric inheritance of fate-determining constituents present in the apical process is sufficient to ensure asymmetric division (Kosodo *et al.*, 2004; Attardo *et al.*, 2008; Bultje *et al.*, 2009), but this notion has been undermined by a recent study showing that even complete inheritance of the apical process is no guarantor of AP fates (Konno *et al.*, 2008). In this context, the status of the basal process has been underexplored, although it has been hypothesized that inheritance of both apical and basal processes is required for self-renewing capability (Konno *et al.*, 2008). Certainly, basal process splitting has been observed to accompany both symmetric and asymmetric neuroepithelial divisions (Kosodo *et al.*, 2008; Kosodo and Huttner, 2009),

although there is controversy whether asymmetric inheritance of the basal process is predictive of neuronal differentiation (Miyata *et al.*, 2001) or progenitor renewal (Ochiai *et al.*, 2009; Alexandre *et al.*, 2010).

In the current study, we set out to explore the role of the basal process, in particular the contribution by the polarized distribution of *Cyclin D2*, in the determination of apical progenitor fate. Previous studies have established that *Cyclin D2* protein localized in the basal process of neural progenitors (Glickstein *et al.*, 2007), and as a member of the *Cyclin* family, may be involved in the regulation of the cell cycle (Dehay and Kennedy, 2007; Salomoni and Calegari, 2010). Other studies have established that another family member, *Cyclin D1*, is implicated in regulating the balance between the number of cortical cells undergoing proliferation or becoming IPs (Lange *et al.*, 2009). Here, we demonstrate using mouse cortical tissue the polarized distribution of *Cyclin D2* mRNA and protein in neural progenitors. We identify a novel 50 base pair (bp) *cis*-acting transport element for the basal localization of *Cyclin D2* mRNA within its 3' untranslated region (3'UTR) and showed that *Cyclin D2* mRNA is locally translated into protein at the basal endfoot. We provide several lines of evidence to suggest that post-transcriptional regulatory systems are required for asymmetric segregation of *Cyclin D2* protein to one of the two daughter cells. In addition, gain- and loss-of-function experiments that perturb asymmetrical distribution of *Cyclin D2* protein in apical progenitor cells severely distort asymmetry of the cell fate. Finally, we show that protein localization of *Cyclin D2* is highly conserved in the human fetal cortex. Taken together, we propose a model for *Cyclin D2* as a fate determinant by the asymmetrical distribution of *Cyclin D2* to the basal process and subsequent inheritance to the mitotic offspring with self-renewing capacity.

Results

Localization patterns of *Cyclin D2* mRNA and protein during early corticogenesis

Localization of *Cyclin D2* protein in the developing neocortex has been previously reported (Ross *et al.*, 1996; Glickstein *et al.*, 2007), while detailed subcellular distributions with regard to developmental periods and cell-cycle phases have not been elucidated. We first examined changes in the expression patterns of *Cyclin D2* mRNA and protein in mouse forebrain during the proliferation (E10.5) and neurogenic stages (E14.5). Antibody specificity was confirmed by western blotting and immunostaining on *Cyclin D2* knockout mouse neocortex with wild-type littermates (Supplementary Figure S1).

From E10.5 to E14.5, *Cyclin D2* mRNA was detected in the cortical wall, mostly near the basal lamina as reported by others, and weakly in the VZ (Figure 1A–C). In comparison, mRNA of other members of the *Cyclin* family, *Cyclin D1* and *Cyclin D3*, was present in the VZ but not at the basal edge of the cortical primordium (Supplementary Figure S2). At higher magnification, expression of *Cyclin D2* mRNA and protein in the cortical wall showed unique and differential patterns. *Cyclin D2* mRNA was preferentially localized in subcellular structures adjacent to the basal lamina at all three stages examined (Figure 1D, F and H). On the other hand, the protein was evenly distributed in cellular nuclei of

the epithelial sheet at E10.5 (Figure 1E), but at older stages (E12.5 and 14.5) the protein showed a dual distribution pattern directed at basal processes and VZ cells with little staining in between (Figure 1G and I). At these stages, *Cyclin D2* protein in the VZ and SVZ was found in the nucleus (arrow in inset of Figure 1G), although not all cells were immunopositive (double arrow in inset of Figure 1G). Even though *Cyclin D2* protein was expressed in nuclear and non-nuclear compartments, *Cyclin D2* mRNA itself was consistently found in cytoplasmic structures on the basal but not apical aspects of the neuroepithelium.

To confirm *Cyclin D2* mRNA and protein were expressed in neural progenitor cells, fluoro *in-situ* hybridization with immunostaining and double immunostaining of *Cyclin D2* mRNA and protein with β III-tubulin (which marks neurons) was performed in the E12.5 cortex. The results show that *Cyclin D2* mRNA and protein localization in basal structures was essentially non-neuronal (Figure 1J and K, arrowheads). Instead, double immunocytochemistry with laminin indicates that *Cyclin D2* staining was not coextensive with the basement membrane (Figure 1L), but restricted in the basal endfoot of neuroepithelial cells revealed by EGFP-lentiviral reporter (Figure 1M and N). Thus, polarized *Cyclin D2* expression in the basal processes of neural progenitors appears during the onset of neurogenesis, and is maintained thereafter.

A *cis*-acting transport element of *Cyclin D2* mRNA resides in its 3' UTR

To elucidate the mechanism behind the polarized distribution of *Cyclin D2* mRNA in cortical progenitor cells, whole-embryo cultures and electroporation experiments were conducted (Supplementary Figure S3A; Osumi and Inoue, 2001). Since localization of mRNA is usually achieved by the binding of a *cis*-acting transport element with a *trans*-acting localization factor (Palacios and St Johnston, 2001), we tested whether a *cis*-acting transport element is present in the 3'UTR of *Cyclin D2* (AK147345). A reporter construct, *pCE/CD2/3'*, was generated by inserting the entire 3'UTR region of *Cyclin D2* mRNA (1106–6274) into an open reading frame (ORF) downstream of *EGFP* in *pCAX*. This construct was co-electroporated with *pCAGGS-mRFP* into the diencephalon of E12.5 embryos, which were subsequently cultured for 12 h (Supplementary Figure S3A). Localization of transcribed mRNAs was detected by *in-situ* hybridization using *EGFP* and *mRFP* riboprobes on adjacent sections from electroporated embryos. The results demonstrate that *EGFP* mRNA fused with a *Cyclin D2* 3'UTR sequence was distributed both in the VZ and in the basal endfoot of neural progenitor cells (Figure 2A), while *mRFP* mRNA without a *Cyclin D2* 3'UTR sequence was present only in the VZ (Figure 2B). This suggests that a *cis*-acting transport element of *Cyclin D2* mRNA is present in its 3'UTR region and is capable of transporting reporter mRNA into the basal endfoot. The speed of this transport event (distance of 400 μ m in the basal process within 12 h) suggests that passive diffusion or lack of mRNA degradation is unlikely to account for the observed polarized distribution of *Cyclin D2* mRNA. Further characterization of this sequence by the use of truncated fragments of the *Cyclin D2* 3'UTR yielded a minimal 50 bp element (*pCE/CD2/3'/3965-4015*) that was sufficient for basal localization of *Cyclin D2* mRNA, both in the diencephalon and in the cortex (Figure 2C and D;

*Corresponding author. Division of Developmental Neuroscience, United Core Centers for Advanced Research and Translational Medicine, Tohoku University School of Medicine, 2-1 Seiryomachi, Aoba-ku, Sendai 980-8575, Japan. Tel.: +81 22 717 8201; Fax: +81 22 717 8205; E-mail: osumi@med.tohoku.ac.jp

Received: 20 June 2011; accepted: 23 January 2012

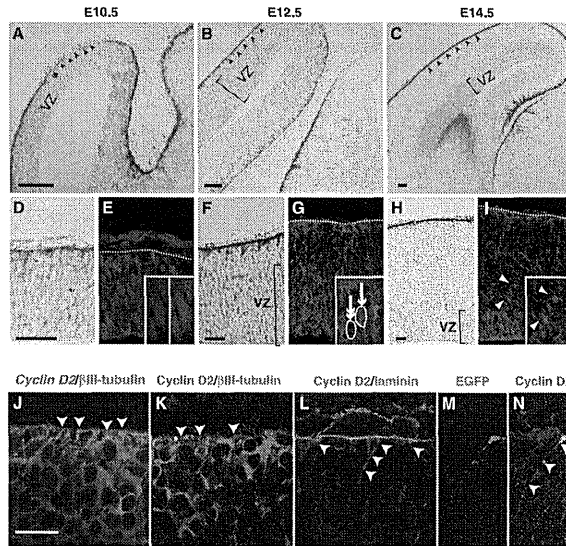


Figure 1 Expression patterns of *Cyclin D2* mRNA and protein during cortical development. (A–I) Localization of *Cyclin D2* mRNA and protein in sections from mouse embryonic neocortex demonstrated by *in-situ* hybridization and immunostaining. At E10.5, *Cyclin D2* mRNA is mainly observed at the basal edge of the neuroepithelium (arrowheads in A, higher magnification in D), whereas *Cyclin D2* protein appears to be uniformly distributed in the nuclei across the epithelial sheet (inset in E). At E12.5 and E14.5, *Cyclin D2* mRNA is preferentially expressed on the basal side of radial glia including the basement membrane (F, H). In contrast, *Cyclin D2* protein is strongly expressed in structures next to the basal lamina (G, I), as well as in the VZ where cells showing strong nuclear staining (inset in G, arrow) are situated next to other cells devoid of *Cyclin D2* protein (inset in G, double arrows). A similar distribution pattern is observed at E14.5 with the additional observation that SVZ cells contain *Cyclin D2* protein (I, arrowheads). (J–L) Double immunostaining in E12.5 cortex shows that *Cyclin D2* mRNA (J) and protein (K) is found in basal endfeet of non-neuronal processes identified by the lack of β III-tubulin (J and K, arrowheads). *Cyclin D2* protein is detected in the apical side of the basal lamina revealed by laminin immunoreactivity (arrowheads in L), and also in the basal process and endfeet of radial glia revealed by EGFP-lentiviral infection (M and N, arrowheads). Dotted lines denote the location of the basal lamina, VZ, ventricular zone. Scale bars: 100 μ m in (A–C), 50 μ m in (D–I), and 20 μ m in (J–N).

Supplementary Figure S3B and C). This finding indicates that a 3'UTR transport element regulates the active transport of *Cyclin D2* mRNA to the basal endfeet.

Transported *Cyclin D2* mRNA is translated locally in the basal endfoot

To examine whether the *Cyclin D2* mRNA in the basal endfeet is translated *in situ*, an expression vector, *pCEN/CD2/3'/1496-5457*, containing EGFP with a nuclear localization signal (NLS-EGFP) was electroporated together with *pCAGGS-mRFP* into E13.5 forebrain *in utero* (Takahashi *et al*, 2002; Figure 3A). A construct containing *Cyclin D2* 3'UTR nucleotides 1496–5457 placed downstream of NLS-EGFP in a reverse direction (*pCEN/CD2/3'/5457-1496*) was used as a control for these experiments (Figure 3A). Following fixation 24 h later, NLS-EGFP mRNA linked to *Cyclin D2* 3'UTR (1496–5457) was observed at the basal endfeet (Figure 3B and B'), while the control mRNA was located only at the VZ with no

polarized distribution to the basal endfeet (Figure 3E and E'). At the protein level, EGFP translated from *pCEN/CD2/3'/1496-5457* was present at the basal endfeet and ventricular nuclei (Figure 3C and C'), whereas EGFP translated from *pCEN/CD2/3'/5457-1496* was present only in nuclei but undetected in the basal endfeet (Figure 3F and F'). From this line of investigation, we predicted that the translated EGFP would be immediately transported into the nucleus via its NLS. However, this is not the case and localization was also noted in the basal endfeet. It has been reported that translation systems, such as ribosomes, are localized at the basal endfeet of the neural progenitor cells (Astrom and Webster, 1991); and therefore, we can conclude that the EGFP observed at the basal endfeet is locally translated and driven by the presence of the *Cyclin D2* 3'UTR. Co-expressed mRFP was seen in the basal processes and basal endfeet, confirming visible observation of the reporter in the endfeet (Figure 3D, D', G, and G').

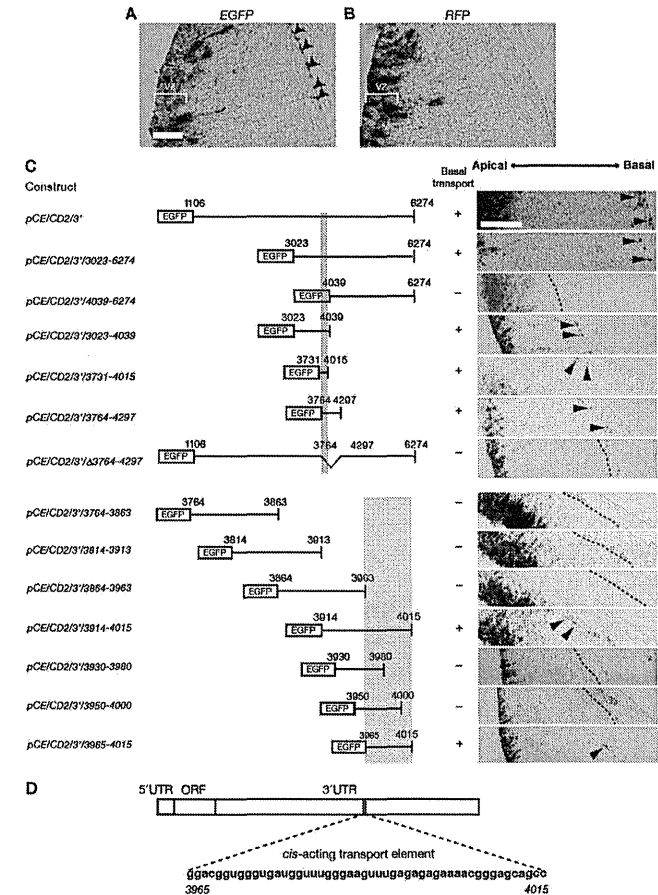


Figure 2 *Cyclin D2* mRNA contains a *cis*-acting transport element in the 3' untranslated region. *In-situ* hybridization for EGFP (A) and RFP mRNA (B), coded by *pCE/CD2/3'* and *pCAGGS-mRFP*, respectively, following electroporation at E12.5. EGFP mRNA is found in the VZ as well as in the basal process and the basal endfeet of the radial glia (arrowheads in A). In contrast, RFP mRNA without *Cyclin D2* 3'UTR is only found in the VZ without expression in the basal process (B). (C) Identification of a 50 nucleotide *cis*-acting mRNA transport element in the *Cyclin D2* 3'UTR. Left panel, regions of the *Cyclin D2* 3'UTR fused with EGFP ORF. Right panel shows localization of EGFP-*Cyclin D2* 3'UTR chimeric mRNA in the mouse diencephalon. (D) Diagrammatic representation of *Cyclin D2* mRNA and *cis*-acting transport element (3965–4015). VZ, ventricular zone. Scale bar: 100 μ m.

Cyclin D2 protein is asymmetrically inherited by one of the two daughter cells

During asymmetric progenitor division, the basal process is inherited by one of its two daughter cells (Miyata *et al*, 2001; Noctor *et al*, 2001). This poses the question of whether the *Cyclin D2* protein is also asymmetrically inherited, and if so,

to which daughter cell does the *Cyclin D2*-containing basal process belong to? To address this, *Cyclin D2* protein was analysed in the basal process and cell body of mitotic offspring revealed by EGFP-lentiviral infection of E11.5 embryos examined 24 h later. The viral titre used was sufficiently low to produce an infected clone (with 1–3 cells) per cortical

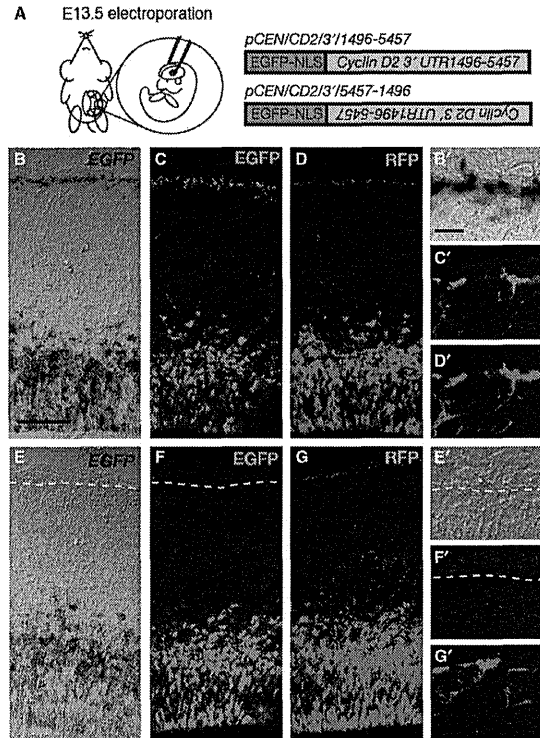


Figure 3 Reporter mRNAs carrying *Cyclin D2* 3'UTR transport element are directed to the basal endfeet and translated locally. (A) EGFP constructs carrying *Cyclin D2* transport element in forward and reverse orientation (*pCEN/CD2/3'/1496-5457* and *pCEN/CD2/3'/5457-1496*) were introduced into the E13.5 mouse neocortex by *in-utero* electroporation, together with *pCAGGS-mRFP*. (B–G) Analysis 24 h later shows that mRNA for EGFP, from *pCEN/CD2/3'/1496-5457*, is expressed at the basal endfeet of radial glia (B and B'). Conversely, EGFP mRNA from *pCEN/CD2/3'/5457-1496* is absent from the basal endfeet (E and E'). At the protein level, EGFP translated from *pCEN/CD2/3'/1496-5457* is present at the basal endfeet and VZ cells (C and C'), whereas EGFP from the reversed *pCEN/CD2/3'/5457-1496* is present only in the VZ but undetected in the basal endfeet (F and F'). Co-transfection with RFP indicates that the reporter protein can be visibly observed in the basal processes and endfeet (D, D', G and G'). Scale bars: 100 μm in (B–G) and 10 μm in (B'–G').

hemisphere, or neighbouring clusters with sufficient separation to be considered as clonal (refer to Supplementary Figure S4). To clearly identify the progenitor cell with its attached basal process, we performed three-dimensional reconstruction of individual daughter cells using Z-stacked images ($n=28$) (a representative image is shown in Supplementary Movie 1). This analysis has revealed that most of the basal processes are inherited by basally positioned daughter cells (26/28) as previously reported (Ochiai *et al.*, 2009).

A transfection protocol was employed to express EGFP in the basal process and immunostaining for Cyclin D2 was

conducted to detect protein distribution at different stages of the cell cycle (Figure 4). Cells in M phase were identified using an antibody against phospho-vimentin (pVim) that stains M-phase cytoplasm and the basal fibres (Figure 4A; Kamei *et al.*, 1998). At the M phase ($n=15$), Cyclin D2 was weakly expressed in the nucleus but strongly expressed in the basal process and endfeet (Figure 4A–D, M, and N). Thus, Cyclin D2 is continuously present in the basal endfeet of APs during the M phase.

To analyse early G1 to late G1 phase, 22 embryos at E12.5 were transfected with the reporter GFP vector. This yielded 19 daughter pairs sharing a single apical process and one basal

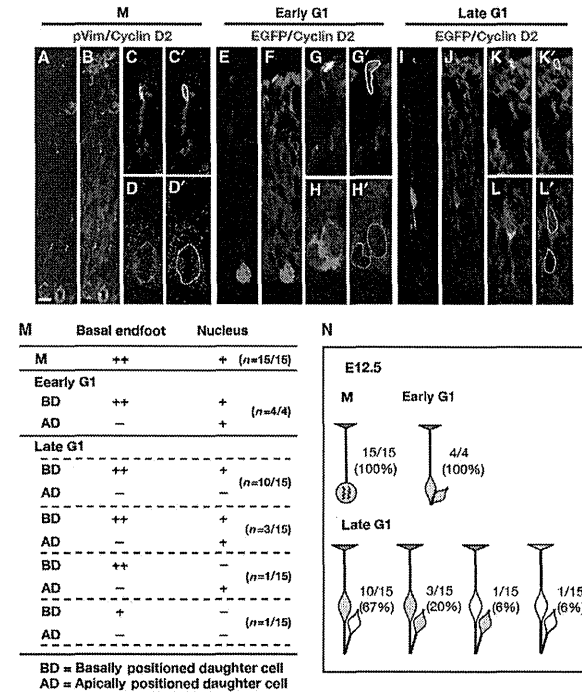


Figure 4 Location and inheritance of Cyclin D2 protein by clonal pairs during the cell cycle at E12.5 using an EGFP lentivirus. (A–D') Identification of clones containing phospho-vimentin-positive M cells show weak Cyclin D2 distribution in the nucleus and basal endfeet. (E–H') A single clone-derived pair of daughter cells anchored by an apical membrane were considered to be in early G1. (G, H') are high-magnification images of centrally positioned cell body and a basal endfeet shown in (C). Cyclin D2 protein at this stage is present in the basal process attached to the basally positioned daughter whose nucleus is also stained for Cyclin D2. The apically positioned daughter is weakly positive for Cyclin D2. (I–L) At late G1, Cyclin D2 is clearly expressed in the basal process and endfeet belonging to the basally positioned daughter (also stained for Cyclin D2). In contrast, the apically positioned daughter is devoid of Cyclin D2. (M) Summary of Cyclin D2 expression in the basal endfeet and nucleus in cells undergoing different stages of the cell cycle. (N) Schematic diagram of Cyclin D2 expression preferential staining of Cyclin D2 in the basal endfeet and nucleus belonging to the basally positioned daughter. Intensity of the staining is shown as + (modest) and ++ (strong). Scale bar: 10 μm.

process inherited by one of the daughter cells and had therefore undergone asymmetric division (Figure 4E–N). To identify early G1 daughter pairs ($n=4$), we used the criterion of close proximity of the daughter cell body to the apical surface (Ochiai *et al.*, 2009), and considered these daughter cells to have been born within a 0–3 h period if one of the two daughters was still anchored to the apical membrane (Figure 4E–H'). This analysis revealed that Cyclin D2 was only weakly expressed in both daughter cell bodies (Figure 4H, H', M, and N), but strongly expressed at the basal process and endfeet (Figure 4G, G', M, and N). By contrast, cells considered to be in late G1 (born greater than 3 h ago and no longer attached to the apical membrane) ($n=15$) showed four dif-

ferent patterns of Cyclin D2 inheritance (Figure 4I–N). In the majority pattern (67%; 10/15), stronger expression of Cyclin D2 was detected in the basally positioned daughter that also carried the basal process stained with Cyclin D2 in the endfeet (Figure 4M and N). Twenty percent of the pairs (3/15) showed equal expression of Cyclin D2 in both daughter cells, and one pair (6%) showed no expression Cyclin D2 in both daughter cells (Figure 4M and N). Finally, another pair (6%) displayed the opposite trend, with strong Cyclin D2 expression in the basal endfeet but no staining in its associated cell body, while the sister cell body without the basal process possessed Cyclin D2 (Figure 4M and N). Thus, Cyclin D2 presents in the basal process and endfeet during cell division, and after asymmetric

cell division, Cyclin D2 is more frequently segregated to the nucleus of the basally positioned daughter cell.

To further examine Cyclin D2 protein inheritance at later stages of neurogenesis (E14.5), E12.5 forebrains were infected with low titre EGFP lentivirus and sacrificed 48 h later (Supplementary Figure S4). Analysis of daughter pairs at early G1 (and therefore closer to the ventricle) showed a variable yet robust result, with 44% of the pairs (4/9) accumulating Cyclin D2 in the basally positioned daughter cell, while the remainder (5/9) showed no detectable Cyclin D2 expression in both daughter cells (Figure 5A–C'' and M). Daughter pairs considered to have undergone division >3 h prior to collection and situated at some distance from the apical membrane were considered to be in late G1. This analysis indicated that 100% of the late G1 daughter pairs (20/20) accumulated more Cyclin D2 protein in the basally positioned daughters (Figure 5D–F'' and M). In summary, these experiments are instructive regarding Cyclin D2 inheritance to daughter cells following apical progenitor divisions during early and mid neurogenesis. Interestingly, compared with earlier stages (E12.5; Figure 4N) a larger proportion of cells at late G1 inherited Cyclin D2 only in the basally

positioned daughter (E14.5; Figure 5M). Taken together, this retrospective staining for Cyclin D2 suggests that preferential distribution of Cyclin D2 protein to one daughter cell is strongly associated with the acquisition of dissimilar daughter cell fates.

Previous studies suggest that apically positioned daughter cells acquire postmitotic neuronal characteristics, while basally positioned daughters tend to be self-renewing (Noctor *et al*, 2001; Konno *et al*, 2008; Ochiai *et al*, 2009). To test this, Ngn2, a marker for neuronal differentiation was used to examine Cyclin D2 inheritance patterns. At E12.5, all the daughter pairs (8/8) at early G1 were devoid of Ngn2 (Supplementary Figure S5A–C and G), a trend also observed at E14.5 (Figure 5G–I'' and N). In contrast to Cyclin D2, 50% of late G1 daughter pairs (9/18) showed Ngn2 accumulation in the apically positioned daughter cell at E12.5 (Supplementary Figure S5D–F and G), and 75% of pairs (12/6) at E14 (Figure 5J–L'' and N). Together, these results strongly point to the conclusion that by late G1, a consequence of asymmetric division is the differential allocation of Cyclin D2 to the nucleus and basal process of the basally positioned daughter cell that is known to undergo self-renewal. In con-

trast, by late G1 Cyclin D2 is invariably absent from the apically positioned daughter cell; these daughter cells acquire Ngn2 in most instances indicating terminal differentiation.

To discount the possibility that asymmetric Cyclin D2 distribution may have arisen from other causes apart from inheritance of locally translated mRNA, two further experiments were performed. The first experiment was to exclude that Cyclin D2 protein may have congregated to one side of the nucleus during M phase, resulting in subsequent asymmetry following division. To check this possibility, E14.5 M-phase neural progenitor cells were double stained with anti-pVim and anti-Cyclin D2 antibodies. The results show that Cyclin D2 protein was only weakly expressed in the nucleus during M phase, and in no case was the distribution asymmetric ($n = 32$) (Supplementary Figure S6A–C). The second possibility is that one of the daughter cells committed for self-renewability may transcribe and translate Cyclin D2 *de novo*. If this is the case, then one of the two daughter cells should exhibit a higher level of Cyclin D2 mRNA. This was not seen in daughter cells labelled with lentiviral infection and stained for Cyclin D2 mRNA by *in-situ* hybridization (Supplementary Figure S6D–F, $n = 6$). Instead, strong expression of Cyclin D2 mRNA was observed at the basal endfeet of the basally positioned daughter cell (Supplementary Figure S6F). As a control, Ngn2 mRNA showed clear asymmetry between daughter cells and was more intense in the apically positioned daughter cell (Supplementary Figure S6G–I').

Disruption of Cyclin D2 asymmetry by acute overexpression or knockdown of gene expression distorts progenitor cell fate

If asymmetrical partitioning of Cyclin D2 protein among mitotic descendants is important for determining cell fate, then systemic alterations of Cyclin D2 levels in neuronal progenitor cells should be expected to disturb the output of asymmetric cell divisions. This would lead to distortions in the ratios of APs, IPs, and differentiated neurons. To induce overexpression of Cyclin D2, pCAX-Cyclin D2-ORF (or control pCAX) was constructed and electroporated *in utero* at E13.5 together with pCAX-EGFP-NLS (to visualize the nucleus). To knockdown Cyclin D2, si1726 or control siRNA was introduced into the E13.5 forebrain by *in-utero* electroporation together with pCAX-EGFP (Supplementary Figure S7A). Overexpression of Cyclin D2 (detectable as increased levels of mRNA and protein of Cyclin D2) in the VZ was clearly visible 24 h later in the vast majority of cells (93.9 ± 0.7%) present in the germinal zones ($n = 3$) (Supplementary Figure S7C, G and J). In comparison, cortices ($n = 3$) electroporated with control plasmid pCAX exhibited Cyclin D2 mRNA and protein in a smaller proportion of cells (53.7 ± 4.1%), representing endogenous levels of Cyclin D2 (Supplementary Figure S7B, F, and J; $P = 0.000346$). Conversely, knockdown of endogenous Cyclin D2 using si1726 produced a reduced number of Cyclin D2 immunopositive cells that was correlated with reduced Cyclin D2 mRNA ($14 \pm 1.3\%$) (Supplementary Figure S7E, I, and J; $n = 3$). It is of note that Cyclin D2 mRNA and protein were diminished from the basal endfeet (Supplementary Figure S7E and inset of Supplementary Figure S7I). As expected, control siRNA electroporated into forebrains ($n = 3$) gave a similar proportion (57.2 ± 1.3%) of endogenously expressing Cyclin D2-positive cells and mRNA expression levels as pCAX control

(Supplementary Figure S7D, H and J; $P = 0.0000147$). We conclude that perturbing Cyclin D2, by overexpression or siRNA knockdown, is capable of disrupting the balance of Cyclin D2 leading to altered fates among daughter cells.

If differential Cyclin D2 levels in mitotic offspring can bias a cell towards a proliferative versus a differentiative fate, then altering Cyclin D2 levels on a global basis will be expected to change global ratios of cells with capacity for self-renewal (AP), further cell division but not renewal (IP), or fully differentiated (postmitotic neuron). Using markers to distinguish between these different cell types that coexist in the neuroepithelial wall, we quantified their relative frequency among EGFP-labelled cells that have become APs (Sox2+ / Tbr2-), or IPs (Tbr2+), or differentiated neurons (SOX2- / Tbr2-) 24 h later (Supplementary Figure S7K–N). The results demonstrate that global overexpression of Cyclin D2 reduced the percentage of non-APs (marked by Tbr2+ or SOX2- / Tbr2- immunostaining) (53.1 ± 1.7% compared with 57.2 ± 1.2% in the control; $P = 0.0527$), but while at the same time increasing the percentage of APs (marked by SOX2+ / Tbr2- staining) (46.9 ± 1.4% compared with 42.6 ± 1% in the control; $P = 0.0527$) (Supplementary Figure S7O). On the other hand, loss-of-function experiment by RNAi knockdown led to increased percentage of neuronal cells (marked by Tbr2+ or SOX2- / Tbr2- immunostaining) (63.9 ± 0.4% compared with 56.9 ± 1.4% in the control; $P = 0.01064$) at the expense of APs (SOX2+ / Tbr2- immunostaining) (36.1 ± 0.4% compared with 43.1 ± 1.4% in the control; $P = 0.01064$) (Supplementary Figure S7O). Thus, widespread expression of Cyclin D2 leads to the increased frequency of AP fates.

To further examine how cell fate was affected by perturbation of Cyclin D2 asymmetry in the longer term, the gain/loss of Cyclin D2 was performed at E12.5, and the location of the EGFP-reporter cells was analysed 48 h after *in-utero* electroporation. We found that overexpression of Cyclin D2 dramatically decreases in the percentage of EGFP+ cells localized to the CP (7.3 ± 0.3% compared with 15.3 ± 0.2% in the control; $P = 0.01069$), while at the same time increasing the percentage of EGFP+ cells in the intermediate zone (IZ) and SVZ (46.9 ± 7.4% compared with 37 ± 0.7% in the control; $P = 0.0541$) (Figure 6A, B, and E). In the loss-of-function experiment, the percentage of EGFP+ cells localized to the CP was proportionally increased (22.3 ± 2.6% compared with 15.4 ± 0.3% in the control; $P = 0.0519$) at the expense of the percentages in the VZ (18 ± 0.7% compared with 20.2 ± 1% in the control; $P = 0.0535$) and SVZ (18 ± 2.7% compared with 23.6 ± 0.5% in the control; $P = 0.0534$) (Figure 6C–E). Therefore, disruption of asymmetrical localization of Cyclin D2 perturbed normal differentiation of neural progenitor cells, while overexpression inhibited neuronal differentiation, loss-of-function promoted neuronal differentiation.

To confirm whether Cyclin D2 conversely promotes cell proliferation, BrdU was pulse labelled for 15 min before sampling. Compared with controls, a larger number of BrdU-labelled cells and mitotic marker PHH3-positive cells were present in the VZ of samples overexpressing Cyclin D2 (Supplementary Figure S8A, B, E, and F), indicating hyperproliferation of neural progenitor cells. Furthermore, ectopic BrdU-labelled cells and PHH3-positive cells were observed in the SVZ and IZ when Cyclin D2 was overexpressed, implying that intermediate progenitors and subventricular radial

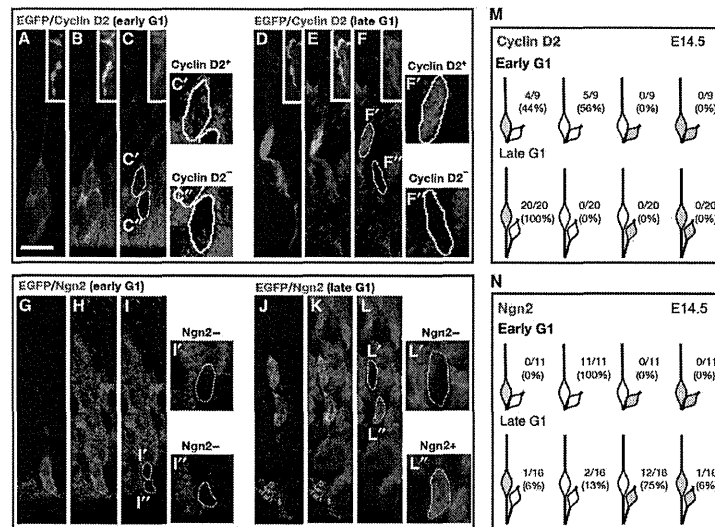


Figure 5 Cyclin D2 protein is asymmetrically inherited by basally positioned daughter cells. (A–C'') Daughter pairs at early G1 (<3 h after mitosis) labelled by EGFP lentivirus at E12.5 and examined at E14.5, inset in (A–F) shows Cyclin D2-positive basal process of radial glia. Higher magnification images (C' and C'') showing preferential allocation of Cyclin D2 to the basally positioned daughter (C'') while the apically positioned daughter (C') is relatively empty of Cyclin D2. Strong expression of Cyclin D2 at the apical side indicates the process of other radial glial cells. (G–I'') At early G1 stage of the cell cycle, Ngn2 was not found in either of the two daughter cells (I' and I''). (D–F'') At late G1 (>3 h after mitosis), daughter pairs positioned next to the apical membrane show preferential staining of Cyclin D2 in the basally positioned daughter cell (F and F''). In contrast, staining for the neuronal marker Ngn2 in a comparable cluster of late G1 daughters (J–L'') demonstrate that Ngn2 is preferentially expressed in the apically positioned daughter (L and L''). (M) Schematic diagram cataloguing the inheritance pattern of Cyclin D2 in late G1 (top row) and early G1 (bottom row). (N) Schematic diagram cataloguing Ngn2 expression in the apically positioned daughter cell in the majority (75%) of late G1 daughter pairs (top row). At early G1, Ngn2 marker is undetectable in either of the daughter cells (bottom row). Scale bar: 10 μm.

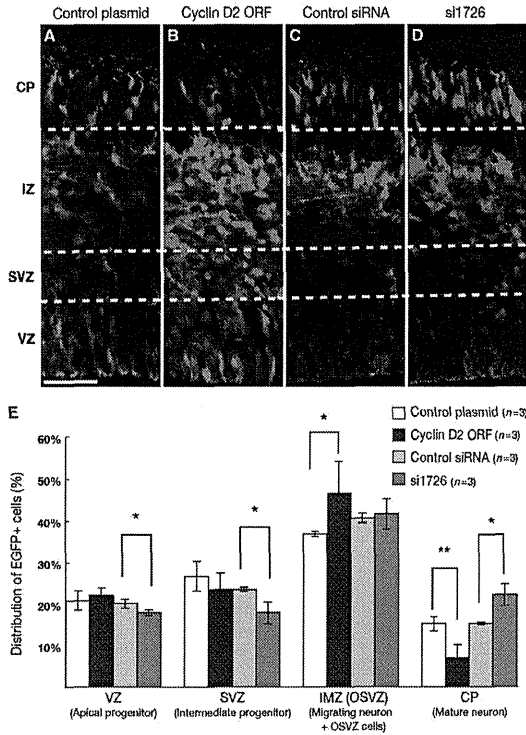


Figure 6 Alterations in cell position resulting from gain/loss of Cyclin D2. Cyclin D2 localization in cells expressing EGFP, 48 h after *in-utero* electroporation at E12.5 with control plasmid (pCAX), pCAX-Cyclin D2-ORF, control Stealth RNAi and Stealth RNAi for mouse Cyclin D2 (si1726) together with pCAX-EGFP. Few EGFP+ cells are observed in the CP of pCAX-Cyclin D2-ORF-electroporated samples (B) compared with control (A). In contrast, more EGFP+ cells are observed in si1726-electroporated samples (D) than in controls (C) at CP. (E) Percentage of EGFP+ cells in the ventricular zone (VZ), subventricular zone (SVZ) and intermediate zone/outer subventricular zone (IMZ/OSVZ) and cortical plate (CP). The VZ is identified as a Tbr2-negative zone and the SVZ identified as a Tbr2-positive zone (data not shown). IZ and CP were distinguished by their morphologies. Error bars indicate s.e.m. * $P < 0.05$, ** $P < 0.01$, Student's *t*-test. Scale bar: 50 μ m.

progenitors may undergo division in response to Cyclin D2 overexpression (Supplementary Figure S8A, B, E, and F). In contrast, downregulation of Cyclin D2 dramatically decreased the number of BrdU-labelled cells and PHH3-positive cells in the VZ and the SVZ relative to controls (Supplementary Figure S8C, D, G, and H). These results confirm that Cyclin D2 is a very strong mitotic cue for neural progenitors.

We have demonstrated the inversely correlated expression patterns of Cyclin D2 and Ngn2 between daughter cells during cortical development (Figures 4N, 5M and N; Supplementary Figure S5). Moreover, the results obtained here revealed that loss of Cyclin D2 expression in the basally positioned daughter cells induced precocious neuronal differ-

entiation (Figure 6E; Supplementary Figure S7O). Thus, all these findings consistently suggest the importance of the asymmetrical distribution of Cyclin D2 protein in the AP cell; specifically, Cyclin D2-negative apical daughter cells will differentiate into neurons, while Cyclin D2-positive basally positioned daughter cells will take on a progenitor fate and proceed to cell division.

Cyclin D2 expression in the developing human cortex
If asymmetric Cyclin D2 partitioning to mitotic offspring is crucial for the determination of self-renewing fate, then one would expect this mechanism to be both ancient and conserved. Since it is not feasible to perform similar perturbation

experiments on human brains, we decided to compare Cyclin D2 protein localization in the human cortex. At 16 and 19 gestational weeks (GW), Cyclin D2 protein was strongly observed at the marginal zone (MZ) and upper part of CP (Figure 7A-C). Cyclin D2 protein was not localized in the nuclei of CP cells, but localized in the basal endfoot of the radial glia in upper CP and MZ (Figure 7C-C'). In the relatively expanded subplate (SP) of the human cortex, punctate Cyclin D2 localization was observed along the glial fibres (Figure 7D-D'). In the VZ and inner SVZ (ISVZ), Cyclin D2 expression was observed in the nucleus of radial glia (Figure 7E-E'). Therefore, the general pattern of Cyclin D2 in humans is remarkably similar to the rodent, suggesting the conservation of this mechanism. Moreover, recent studies have identified new sub-populations of proliferative cells in the outer SVZ in the fetal human and ferret brains; these cells are distinguished by their possession of basal but not apical processes (Fietz et al, 2010; Hansen et al,

2010). Examination of cortical tissue at 19 GW confirmed that Cyclin D2 was present in cells of the OSVZ, and in addition, also present in the basal process (Figure 7F-H, insets). At the genetic level, it is noteworthy that human Cyclin D2 mRNA (NM-001759) also contains a predicted 50 bp transport element in the 3'UTR (with 74% sequence match to the mouse), raising the possibility that basal transport of human Cyclin D2 mRNA for local translation in the basal process may also be operative.

Discussion

During corticogenesis, the cells that populate the expanding cortical wall comprise a heterogeneous mixture of dividing and non-dividing cells. This balance is necessary to ensure that the correct number of neurons are generated at an appropriate stage, and at the same time, maintaining a pool of self-renewing progenitors. To achieve this, progenitors

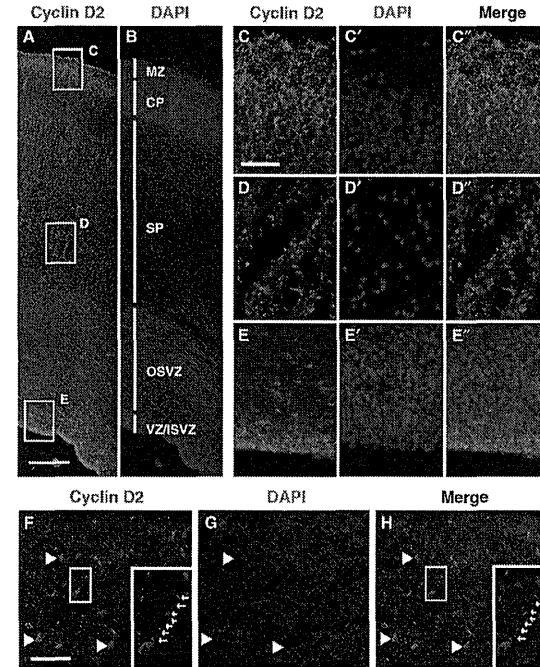


Figure 7 Cyclin D2 protein is expressed in the developing human cortex. (A-E') At 16 GW, Cyclin D2 is expressed at three principal locations: the basal aspects of the CP near the MZ (box C); the subplate (box D), and the apical aspects of the VZ (box E). At higher magnification, Cyclin D2 in the basal aspects and the subplate are present in a punctate fashion along the cellular processes and not in the cell nuclei stained with DAPI (C, D). In the VZ, Cyclin D2 staining colocalizes with nuclei of neural progenitor cells (E). (F-H) Localization of Cyclin D2 protein in SP and OSVZ regions of the 19 GW human cortex showing Cyclin D2 staining in cells and also in a long basal process (F and H; arrows in insets). MZ, marginal zone; CP, cortical plate; SP, subplate; OSVZ, outer subventricular zone; VZ/ISVZ, ventricular zone/inner subventricular zone. Scale bars: 100 μ m in (A and B), 25 μ m in (C-E'), and 50 μ m in (F-H).

undergo both symmetric and asymmetric cell divisions, but these events are classified by their outcomes rather than by their prior appearance or behaviour. While it is still not possible to forecast whether a progenitor will undergo symmetric or asymmetric division, a number of studies have attempted to link the mode of division with the acquisition of certain cellular and molecular characteristics. For example, cleavage plane orientation has been suggested to be a key factor (Chenn and McConnell, 1995; Zhong *et al*, 1996), but the low frequency of horizontal cleavage planes in the proliferative wall is irreconcilable with the large number of cortical neurons that needs to be produced (Huttner and Brand, 1997). While cleavage plane orientation is now considered to be unrelated to the mode of cell division (Attardo *et al*, 2008; Noctor *et al*, 2008), fate determinants such as Numb, present at the apical border, and TRIM32, present at the basal side of the cell body, appear to be preferentially inherited by the terminally differentiating daughter (Shen *et al*, 2002; Schwamborn *et al*, 2009). Other proteins found at the apical membrane, such as the Par complex (Costa *et al*, 2008; Bulthé *et al*, 2009), have been implicated for controlling the balance between self-renewing and non-self-renewing divisions. By contrast, proteins enriched at the basal end of the progenitor have been less well studied as potential regulators of asymmetric versus symmetric cell division.

In this study, we revealed that allocation of Cyclin D2 to the tip of the basal process and its subsequent inheritance to the basally positioned daughter cell is strongly associated with the acquisition of a self-renewing fate of the AP. During mitosis the apically positioned daughter cell, expressing Ngn2, will adopt a different fate as a neuron or an IP (Figure 8). In summary, Cyclin D2 is expressed in the basal endfoot and nucleus, but by G1, it begins to be partitioned from the inherited basal process to the self-renewing daughter cell of the AP during an asymmetric division event. By late G1, asymmetric partitioning of Cyclin D2 becomes a hallmark for the basally positioned progenitor that is invariably non-neuronal (Ngn2 negative). Despite the first sign of Cyclin D2 asymmetry appearing in G1 pairs still attached to the apical surface, the majority of such daughter pairs either show equally weak Cyclin D2 distribution, or no Cyclin D2 whatsoever in both daughters. Interestingly, these daughter pairs rarely stain with Ngn2, suggesting the fate of each daughter cell remained uncommitted in this period.

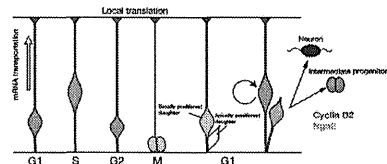


Figure 8 Schematic depiction of *Cyclin D2* mRNA and protein localization during the cell cycle and its putative role as a fate determinant. Pink and blue colours indicate Cyclin D2 and Ngn2 localization in the radial glia, respectively. *Cyclin D2* mRNA is transported to the basal endfoot during S-to-G2 phase (light pink arrow) and translated into protein. During mitosis, *Cyclin D2* mRNA or protein is inherited by the basally positioned daughter cell that assumes an apical progenitor fate.

If asymmetric distribution of Cyclin D2 is required for asymmetric cell fate determination, then Cyclin D2 overexpression should increase the frequency of symmetric cell divisions leading to increased numbers of APs, with concomitant reductions in numbers of differentiated neurons. These effects were observed with Cyclin D2 overexpression, and the opposite results obtained using RNAi knockdown experiments (Supplementary Figure S7O). Notably, this knockdown almost depleted mRNA and protein of Cyclin D2 from the endfoot, and produced a greater impact on the cell fate of neural progenitors compared with overexpression experiments. In summary, localization of Cyclin D2 in the basal endfoot has a critical role in the process of early corticogenesis.

An interesting aspect of Cyclin D2 is the strategy employed for unequal inheritance. Unlike Numb where the protein is preferentially allocated to the neuronal daughter (Shen *et al*, 2002), Cyclin D2 relies on transport of its mRNA during the S-to-G2 phase to the basal endfoot, where it is locally translated. This strategy relies on a 50-bp *cis*-acting transport element, present in full-length transcripts of *Cyclin D2* for translation into a 32-kDa protein (Denicourt *et al*, 2003), which is both necessary and sufficient for basal transport of fluorescent reporters. Importantly, this unique element is neither present in mouse *Cyclin D1* (Supplementary Figure S2) nor in chick *Cyclin D2* (NM-204213), both of which do not show asymmetric expression patterns in the developing forebrain. Sequence analysis of small RNAs do not exclude the possibility (Wang, 2008; Wang and El Naqa, 2008) that Cyclin D2 could be a potential target of certain microRNAs (e.g., mir-1192 and mir-495), but it remains unknown whether miRNA activity can be spatially distinctive enough to cause unequal distribution of *Cyclin D2* mRNA and protein in the endfoot. Moreover, a clear difference in Cyclin D2 protein levels between daughter cells is produced after cell division.

It has been mooted that inheritance of the basal process is associated with, and required for, asymmetric divisions (Konno *et al*, 2008). If that is correct, what then might be the mechanism that leads Cyclin D2 in the basal process to favour an AP fate? One possibility is that the long basal process increases the temporal interval for Cyclin D2 in the endfoot to gain access to the nucleus at G1. It is known that neural progenitors elongate their G1 phases during corticogenesis (Takahashi *et al*, 1995) and that progenitors at G1 are vulnerable to fate-determining events (McConnell and Kaznowski, 1991). Thus, delaying the interval of exposure to the nucleus by fate determinants such as Cyclin D2 may generate effects that are akin to shortening the G1 phase, thereby preventing the recipient nucleus from assuming a neuronal fate and favouring an AP fate. Indeed, artificial elongation of the G1 phase by another family protein, Cyclin D1, causes premature neurogenesis (Calegari and Huttner, 2003), while removal of Cyclin D2 gene by deletion causes G1 lengthening, leading to early exit from the cell cycle and encouraging neuronal differentiation (Glickstein *et al*, 2009). In that study, *Cyclin D2* knockout mice exhibit microcephaly and thinner cortical walls (Glickstein *et al*, 2009), features consistent with the present hypothesis that Cyclin D2 is crucial for maintaining divisions of APs.

In the present study, the increased focus on the basal process for AP fate has parallels in primates. In the outer SVZ of human, ferret, and mouse cortices, a new population of proliferative cells have recently been reported to have basal

processes but not apical processes and divide asymmetrically to produce one progenitor and one neuronal cell (Fietz *et al*, 2010; Hansen *et al*, 2010; Reillo *et al*, 2010; Wang *et al*, 2011). In addition, it has been reported that the basal process is instrumental for relaying a retinoic acid signal from the meninges to control progenitor cell proliferation (Siegenthaler *et al*, 2009). Given that we observe broad similarities in Cyclin D2 protein expression between developing mouse and human cortices, it is worth postulating that despite 70 million years of evolutionary divergence, the role of Cyclin D2 in maintaining AP renewal may be operative in all mammalian species. Furthermore, given its capacity to influence progenitor cell renewal, Cyclin D2 lends itself for evolutionary selection to increase the number of cell cycles (known to occur in primates) for generating a larger cortex (Finlay and Darlington, 1995; Rakic, 1995; Dehay and Kennedy, 2007), or within a given area of the cortex to generate more neurons for increased architectonic complexity (Dehay *et al*, 1993).

Materials and methods

Animals

Animal experiments were carried out in accordance with the National Institutes of Health Guide for the Care and Use of Laboratory Animals. The Committee for Animal Experimentation of the Tohoku University Graduate School of Medicine approved the experimental procedures described herein. The midday of the vaginal plug was designated as embryonic day 0.5 (E0.5). Pregnant ICR mice were purchased from Charles River Japan (Yokohama, Japan). *Cyclin D2* knockout mice were kindly obtained from Dr Scicinski (Scicinski *et al*, 1996).

Fetal tissue collection

Human fetal brain tissue was obtained from the NSW Fetal Tissue Consortium with approval from the University of Sydney Human Research Ethics Committee and the Melbourne Health Human Research Ethics Committee. This work was carried out under the NHMRC National Statement on Ethical Conduct in Human research. Gestation age of fetus ranged between 16 and 19 weeks. Brain tissue was dissected and transported in ice-cold HEPES-buffered MEM (Invitrogen, Carlsbad, CA) and fixed in 4% paraformaldehyde (PFA) (w/v) in 0.1 M phosphate buffer (PB) for 1–9 h at 4°C. Fixed tissue was dehydrated in 20% sucrose in PB, embedded and frozen at –80°C in O.C.T compound (Tissue-Tek) and cryosectioned.

Staining procedures

In-situ hybridization and immunostaining procedures were performed according to methods previously described (Takahashi and Osumi, 2002). Antibodies used are listed in Supplementary Table 1. Information about probes, primers, and antibodies are supplied in Supplementary data.

Expression constructs

All expression constructs used in this study were cloned in frame into pCAX expression vector, a modified version of pCAGGS, in which multicloning site was inserted and the SV40 origin was deleted (kindly provided by the late K Umesono). All constructs were verified by sequence analysis. The entire mouse *Cyclin D2* cDNA (RIKEN MOUSE FANTOM, GenBank accession number AK14745) was obtained from DANAFORM (Yokohama, Japan).

References

Alexandre P, Reutegels AM, Barker D, Blanc E, Clarke JD (2010) Neurons derive from the more apical daughter in asymmetric divisions in the zebrafish neural tube. *Nat Neurosci* 13: 673–679

For the *cis*-acting transport element assay, parts of the *Cyclin D2* 3'UTR sequence were subcloned into pCAX-EGFP downstream of the EGFP sequence.

Gene transfer into mouse embryos by electroporation

The experimental procedures for whole-embryo culture and electroporation have been described previously (Osumi and Inoue, 2001; Takahashi *et al*, 2008). The pCAGGS-mRFP vector was kindly provided by Dr Masanori Uchikawa. The pCAX-Cyclin D2-ORF was generated by the insertion of PCR-amplified ORF into the pCAX vector. The stealth RNAi against mouse *Cyclin D2* (S1726, UUAGGUAGCAGCUUAGUCAGC) and the scramble control RNAi (SiCr, UUACUGGAGCGACUCUAUGAUAGC) were purchased from Invitrogen and used in 200 µg/µl phosphate buffer saline (PBS) solution.

Virus production and injection into the brain

EGFP lentivirus was produced using pCS-EF-EGFP, pCMV-VSV-G-RSV-Rev, and pCAG-HIVgp plasmids, which were kindly provided by Dr Miyoshi as described previously (Tahara-Hanaoka *et al*, 2002). For details, see Supplementary data.

Statistical analysis

The quantitative data were evaluated by Student's *t*-test, using Excel 2004 for Mac (Microsoft, WA, USA), and presented as mean ± s.e.m.

Supplementary data

Supplementary data are available at *The EMBO Journal* Online (<http://www.embojournal.org>).

Acknowledgements

We thank Drs Takaki Miyata and Yoichi Kosodo and Tadashi Nomura for a critical reading of the manuscript and valuable comments. We thank Drs Federico Calegari, Atsunori Shitamukai and Takashi Takeuchi for valuable suggestions on our work. We also thank Dr Hiroyuki Miyoshi for the lentivirus vectors, Dr Masanori Uchikawa for the pCAGGS-mRFP vector, and Dr Hiroto Okayama for rat *Cyclin D1* cDNA, Dr DJ Anderson for Ngn2 antibody, Dr Masato Nakafuku for Ngn2 probe, Dr Peter Scicinski for *Cyclin D2* knockout mouse. We are grateful to Ms Ayumi Ogasawara for animal care and Ms Sayaka Makino and Ms Makiko Sasaki-Hoshino for technical support. We thank all other members of the Osumi laboratory for their valuable discussions and hearty encouragement. The use of discarded human brain tissue was approved by Human Research Ethics Committee, Melbourne Health, Australia. This work was supported by KAKENHI (#17024001 to NO and #17700300 to MT) from MEXT, by CREST from the Japan Science and Technology Agency (JST) (to NO), the Global COE Program "Basic and Translational Research Center for Global Brain Science" of MEXT of Japan (to NO), and by the Australian National Health and Medical Research Council. YT was supported by the GCOE program as a GCOE fellow.

Author contributions: YT, MT, and NO designed the experiments. MT designed and characterized the Ngn2 antibody, and YT carried out all other experiments except Figure 7, which was performed by JMB and S-ST. YT, JMB, MT, FP, S-ST, and NO discussed the results and wrote the manuscript. All authors read and approved the final manuscript.

Conflict of interest

The authors declare that they have no conflict of interest.

- Attardo A, Calegari F, Haubensak W, Wilsch-Brauninger M, Huttner WB (2008) Live imaging at the onset of cortical neurogenesis reveals differential appearance of the neuronal phenotype in apical versus basal progenitor progeny. *PLoS One* 3: e2386
- Bultje RS, Castaneda-Castellanos DR, Jan LY, Jan YN, Kriegstein AR, Shi SH (2009) Mammalian Par3 regulates progenitor cell asymmetric division via notch signaling in the developing neocortex. *Neuron* 63: 189–202
- Calegari F, Huttner WB (2003) An inhibition of cyclin-dependent kinases that lengthens, but does not arrest, neuroepithelial cell cycle induces premature neurogenesis. *J Cell Sci* 116(Part 24): 4947–4955
- Chenn A, McConnell SK (1995) Cleavage orientation and the asymmetric inheritance of Notch1 immunoreactivity in mammalian neurogenesis. *Cell* 82: 631–641
- Costa MR, Wen G, Lepier A, Schroeder T, Gotz M (2008) Par-complex proteins promote proliferative progenitor divisions in the developing mouse cerebral cortex. *Development* 135: 11–22
- Dehay C, Giroud P, Berland M, Smart I, Kennedy H (1993) Modulation of the cell cycle contributes to the parcellation of the primate visual cortex. *Nature* 366: 464–466
- Dehay C, Kennedy H (2007) Cell-cycle control and cortical development. *Nat Rev Neurosci* 10: 438–450
- Denicourt C, Kozak CA, Rassart E (2003) Grisl, a new common integration site in Graffi murine leukemia virus-induced leukemias: overexpression of a truncated cyclin D2 due to alternative splicing. *J Virol* 77: 37–44
- Fietz SA, Kelava I, Vogt J, Wilsch-Brauninger M, Stenzel D, Fish JL, Corbeil D, Riehn A, Distler W, Niisch R, Huttner WB (2010) OSVZ progenitors of human and ferret neocortex are epithelial-like and expand by integrin signaling. *Nat Neurosci* 13: 690–699
- Finlay BL, Darlington RB (1995) Linked regularities in the development and evolution of mammalian brains. *Science* 268: 1578–1584
- Glickstein SB, Alexander S, Ross ME (2007) Differences in cyclin D2 and D1 protein expression distinguish forebrain progenitor subtypes. *Cereb Cortex* 17: 632–642
- Glickstein SB, Monaghan JA, Kneller JB, Jones TK, Ross ME (2009) Cyclin D2 is critical for intermediate progenitor cell proliferation in the embryonic cortex. *J Neurosci* 29: 9614–9624
- Gotz M, Huttner WB (2005) The cell biology of neurogenesis. *Nat Rev* 6: 777–788
- Hansen DV, Lui JH, Parker PR, Kriegstein AR (2010) Neurogenic radial glia in the outer subventricular zone of human neocortex. *Nature* 464: 554–561
- Haubensak W, Attardo A, Denk W, Huttner WB (2004) Neurons arise in the basal neuroepithelium of the early mammalian telencephalon: a major site of neurogenesis. *Proc Natl Acad Sci USA* 101: 3196–3201
- Huttner WB, Brand M (1997) Asymmetric division and polarity of neuroepithelial cells. *Curr Opin Neurobiol* 7: 29–39
- Huttner WB, Kosodo Y (2005) Symmetric versus asymmetric cell division during neurogenesis in the developing vertebrate central nervous system. *Curr Opin Cell Biol* 17: 648–657
- Kamei Y, Inagaki N, Nishizawa M, Tsutsumi O, Taketani Y, Inagaki M (1998) Visualization of mitotic radial glial lineage cells in the developing rat brain by Cdc2 kinase-phosphorylated vimentin. *Glia* 23: 191–199
- Konno D, Shiota G, Shtiamukai A, Mori A, Kiyonari H, Miyata T, Matsuzaki F (2008) Neuroepithelial progenitors undergo LGN-dependent planar divisions to maintain self-renewability during mammalian neurogenesis. *Nat Cell Biol* 10: 93–101
- Kosodo Y, Huttner WB (2009) Basal process and cell divisions of neural progenitors in the developing brain. *Dev Growth Differ* 51: 251–261
- Kosodo Y, Roper K, Haubensak W, Marzescu AM, Corbeil D, Huttner WB (2004) Asymmetric distribution of the apical plasma membrane during neurogenic divisions of mammalian neuroepithelial cells. *EMBO J* 23: 2314–2324
- Kosodo Y, Toida K, Dubreuil V, Alexandre P, Schenk J, Kiyokage E, Attardo A, Mora-Bermudez F, Arii T, Clarke JD, Huttner WB (2008) Cytokinesis of neuroepithelial cells can divide their basal process before anaphase. *EMBO J* 27: 3151–3163
- Kriegstein A, Noctor S, Martinez-Cerdeno V (2006) Patterns of neural stem and progenitor cell division may underlie evolutionary cortical expansion. *Nat Rev Neurosci* 7: 883–890
- Lange C, Huttner WB, Calegari F (2009) Cdk4/cyclinD1 overexpression in neural stem cells shortens G1, delays neurogenesis, and promotes the generation and expansion of basal progenitors. *Cell Stem Cell* 5: 320–331
- McConnell SK, Kazanowski CE (1991) Cell cycle dependence of laminar determination in developing neocortex. *Science* 254: 282–285
- Miyata T, Kawaguchi A, Okano H, Ogawa M (2001) Asymmetric inheritance of radial glial fibers by cortical neurons. *Neuron* 31: 727–741
- Miyata T, Kawaguchi A, Saito K, Kawano M, Muto T, Ogawa M (2004) Asymmetric production of surface-dividing and non-surface-dividing cortical progenitor cells. *Development* 131: 3133–3145
- Noctor SC, Flint AC, Weissman TA, Dammerman RS, Kriegstein AR (2001) Neurons derived from radial glial cells establish radial units in neocortex. *Nature* 409: 714–720
- Noctor SC, Martinez-Cerdeno V, Ivic L, Kriegstein AR (2004) Cortical neurons arise in symmetric and asymmetric division zones and migrate through specific phases. *Nat Neurosci* 7: 136–144
- Noctor SC, Martinez-Cerdeno V, Kriegstein AR (2008) Distinct behaviors of neural stem and progenitor cells underlie cortical neurogenesis. *J Comp Neurol* 508: 28–44
- Ochiai W, Nakatani S, Takahara T, Kainuma M, Masaoka M, Minobe S, Namiura M, Nakashima K, Sakakibara A, Ogawa M, Miyata T (2009) Periventricular notch activation and asymmetric Ngn2 and Tbr2 expression in pair-generated neocortical daughter cells. *Mol Cell Neurosci* 40: 225–233
- Osumi N, Inoue T (2001) Gene transfer into cultured mammalian embryos by electroporation. *Methods* 24: 35–42
- Palacios IM, St Johnston D (2001) Getting the message across: the intracellular localization of mRNAs in higher eukaryotes. *Annu Rev Cell Dev Biol* 17: 569–614
- Rakic P (1988) Specification of cerebral cortical areas. *Science* 241: 170–176
- Rakic P (1995) A small step for the cell, a giant leap for mankind: a hypothesis of neocortical expansion during evolution. *Trends Neurosci* 18: 383–388
- Reille I, de Juan Romero C, Garcia-Cabezas MA, Borrell V (2010) A role for intermediate radial glia in the tangential expansion of the mammalian cerebral cortex. *Cereb Cortex* 21: 1674–1694
- Ross ME, Carter ML, Lee JH (1996) MN20, a D2 cyclin, is transiently expressed in selected neural populations during embryogenesis. *J Neurosci* 16: 210–219
- Salomoni P, Calegari F (2010) Cell cycle control of mammalian neural stem cells: putting a speed limit on G1. *Trends Cell Biol* 20: 233–243
- Schwamborn JC, Berezikov E, Knoblich JA (2009) The TRIM-NHL protein TRIM52 activates microRNAs and prevents self-renewal in mouse neural progenitors. *Cell* 136: 913–925
- Shen Q, Zhong W, Jan YN, Temple S (2002) Asymmetric Numb distribution is critical for asymmetric cell division of mouse cerebral cortical stem cells and neuroblasts. *Development* 129: 4843–4853
- Sicinski P, Donaher JL, Geng Y, Parker SB, Gardner H, Park MY, Robker RL, Richards JS, McGinnis LK, Biggers JD, Eppig JJ, Bronson RT, Elledge SJ, Weinberg RA (1996) Cyclin D2 is an FSH-responsive gene involved in gonadal cell proliferation and oncogenesis. *Nature* 384: 470–474
- Siegenthaler JA, Ashique AM, Zarbalis K, Patterson KP, Hecht JH, Kane MA, Polias AE, Choe Y, May SR, Rume T, Napoli JL, Peterson AS, Pleasure SJ (2009) Retinoic acid from the meninges regulates cortical neuron generation. *Cell* 139: 597–609
- Smart IH (1973) Proliferative characteristics of the ependymal layer during the early development of the mouse neocortex: a pilot study based on recording the number, location and plane of cleavage of mitotic figures. *J Anat* 116(Part 1): 67–91
- Tahara-Hanaoka S, Sudo K, Ema H, Miyoshi H, Nakauchi H (2002) Lentiviral vector-mediated transduction of murine CD34(+) hematopoietic stem cells. *Exp Hematol* 30: 11–17
- Takahashi M, Nomura T, Osumi N (2008) Transferring genes into cultured mammalian embryos by electroporation. *Dev Growth Differ* 50: 485–497
- Takahashi M, Osumi N (2002) Pax6 regulates specification of ventral neurone subtypes in the hindbrain by establishing progenitor domains. *Development* 129: 1327–1338
- Takahashi M, Sato K, Nomura T, Osumi N (2002) Manipulating gene expressions by electroporation in the developing brain of mammalian embryos. *Differentiation* 70: 155–162
- Takahashi T, Nowakowski RS, Caviness Jr VS (1995) The cell cycle of the pseudostratified ventricular epithelium of the embryonic murine cerebral wall. *J Neurosci* 15: 6046–6057
- Wang X (2008) miRDB: a microRNA target prediction and functional annotation database with a wiki interface. *RNA* 14: 1012–1017
- Wang X, El Naqa IM (2008) Prediction of both conserved and nonconserved microRNA targets in animals. *Bioinformatics* 24: 325–332
- Wang X, Tsai JW, LaMonica B, Kriegstein AR (2011) A new subtype of progenitor cell in the mouse embryonic neocortex. *Nat Neurosci* 14: 555–561
- Zhong W, Feder JN, Jiang MM, Jan LY, Jan YN (1996) Asymmetric localization of a mammalian numb homolog during mouse cortical neurogenesis. *Neuron* 17: 43–53

Evaluation of Vortex Flow in Left Ventricle by Echo-dynamography and Phase Contrast Magnetic Resonance Angiography

Takanori Kojima, Takeyoshi Kameyama, Hiroyuki Nakajima, Elena Khmyrova, Takafumi Kurokawa, Yoshifumi Saijo, *Member, IEEE*

Abstract— Echo-dynamography (EDG) is a method for visualizing left ventricular (LV) blood flow based on cardiac Doppler measurement in which blood flow component perpendicular to the ultrasonic beam is deduced by applying fluid dynamics theories to two-dimensional (2D) distribution of blood flow component along the ultrasonic beam. EDG has been validated by numerical simulation and particle image velocimetry of model circulation. However, these validations were too simple to reproduce unstable and asymmetrical flow in a beating heart. In the present study, EDG is compared with three-directional (3D) blood flow distribution on the same plane obtained with phase contrast magnetic resonance angiography (PC-MRA) for clinical validation. Moreover, the location and vorticity of the vortex flow in LV are measured quantitatively and the relation to echocardiographic parameters of systolic and diastolic functions is discussed.

3D components of blood flow on a plane were obtained with triple scans of the same plane with ECG trigger and breath holding; 1) phase encode (x-axis), 2) read out (y-axis) and 3) slice selection (z-axis). After the acquisition of MRA dataset, color Doppler dataset of the same plane was acquired and 2D velocity distribution was obtained with EDG in MATLAB programs.

EDG and PC-MRA showed similar velocity vector distribution and formation of LV vortex flow. The vortex at mid diastolic phase was strongly affected by early diastolic filling while the vortex at isometric contraction was affected by atrial filling. EDG gained a new insight on systolic-diastolic coupling from the view point of LV blood flow such as LV vortex formation.

I. INTRODUCTION

ACCORDING to the Frank-Starling law, the stroke volume of the heart increases in response to an increase in the volume of blood filling the heart (the end diastolic volume). Thus, cardiac pump function is determined how long the myocardium stretches in end-diastole. Left ventricular (LV)

Manuscript received March 28, 2012. This project was supported in part by Grants-in-Aid for Scientific Research (Scientific Research (B) 22300175, Challenging Exploratory Research 23650300) from the Japan Society for the Promotion of Science, Sendai Advanced Preventive Health Care Services Cluster from the Ministry of Education, Culture, Sports, Science and Technology and Regional Innovation Program from the Ministry of Economy, Trade and Industry.

Takanori Kojima (e-mail: takanori.kojima@bme.tohoku.ac.jp), Hiroyuki Nakajima (e-mail: hiro1029@sea.plala.or.jp), Elena Kymhrova (e-mail: elena.kymhrova@bme.tohoku.ac.jp), and Yoshifumi Saijo (phone: +81-22-717-8514; fax: +81-22-795-7149; e-mail: saiyo@idac.tohoku.ac.jp) are with the Graduate School of Biomedical Engineering, Tohoku University, Sendai 980-8579 Japan.

Takeyoshi Kameyama (e-mail: takeyosh@wa2.so-net.ne.jp) and Takafumi Kurokawa (e-mail: nenkin_kurokawa@yahoo.co.jp) are with the Graduate School of Medical Sciences, Tohoku University, Sendai 980-8575 Japan.

diastolic function apparently affects LV systolic function. In clinical settings, diastolic function is often measured as well as systolic pump function such as LV ejection fraction (EF). Recently, the concept of “diastolic heart failure [1]” or “heart failure with preserved EF” has been proposed and diastolic function is believed to deteriorate prior to the deterioration of systolic function.

Myocardial tissue Doppler imaging can measure longitudinal myocardial velocities of the mitral annulus; (1) s', systolic myocardial velocity above the baseline as the annulus descends toward the apex; (2) e', early diastolic myocardial relaxation velocity below the baseline as the annulus ascends away from the apex; and (3) a', myocardial velocity associated with atrial contraction. The strong correlation between s' and e' may indicate systolic-diastolic coupling in short term relationship from a view of physiology of cardiac myocytes. On the other hand, evaluation of cardiac function has been performed by intracardiac blood flow measurement. For example, diastolic function was assessed by early diastolic filling (E) over atrial filling (A) ratio and most suitable parameters of CRT (cardiac resynchronization therapy) is set to maximize velocity-time integral of left ventricular outflow.

The blood flow structure in whole LV has been assessed by echo-dynamography (EDG) [2-5]. EDG is a method for visualizing left ventricular (LV) blood flow based on cardiac Doppler measurement in which blood flow component perpendicular to the ultrasonic beam is deduced by applying fluid dynamics theories to two-dimensional (2D) distribution of blood flow component along the ultrasonic beam. EDG has been validated by numerical simulation [6] and particle image velocimetry of model circulation. However, these validations were too simple to reproduce unstable and asymmetrical flow in a beating heart.

In the present study, EDG is compared with three-directional (3D) blood flow distribution on the same plane obtained with phase contrast magnetic resonance angiography (PC-MRA) for clinical validation. Moreover, the location and vorticity of the vortex flow in LV are measured quantitatively and the relation to echocardiographic parameters of systolic and diastolic functions is discussed.

II. METHODS

A. Echo-dynamography

A Color Doppler movie of the apical three-chamber view containing LV apex, center of mitral leaflets, and center of

aortic valve was recorded in a commercially available ultrasound machine (SSD-6500SV, Aloka, Tokyo, Japan) in the left lateral recumbent position. The central frequency was 2.5 MHz and the frame rate was 10 fps.

Fig. 1 shows the concept of EDG. Blood flow is separated into two kinds of flow; vortex on a 2D plane and basic flow in the 3D space.

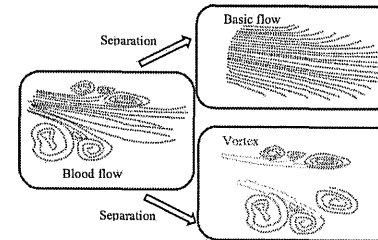


Fig. 1 Principle of echo-dynamography. Vortex components on a 2D plane and basic flow components in the 3D space are separated.

The processing algorithm of EDG consists of four steps.

Step1: The color Doppler data are decomposed into basic and vortex flow components such that the velocity profile of each vortex flow component is bilaterally symmetric.

Step2: In the vortex flow component, tangential velocities are found using stream function on an assumption that the velocity components perpendicular to the scan plane are zero.

Step3: In the basic flow component, the directions of flow vectors are found using flow function [2]. Tangential velocities can be found from the directions of flow vectors and the basic flow component of the color.

Step4: The velocity vector field is generated by composing the vectors from the two components.

EDG was obtained by these steps on MATLAB.

B. Phase Contrast Magnetic Resonance Angiography

All PC-MRA data acquisitions were performed using a 1.5-Tesla MRI scanner (EXCELART Vantage MRT200-PP5; Toshiba Medical, Japan).

MR flow data were obtained from apical three chamber images. 2D PC-MRA data was acquired with the following parameters: repetition time 24 msec, echo time 10 msec, flip angle 20 degree and 8-mm slice thickness. The velocity-encoding gradient value was 100cm/s, and three-directional (3D) components of blood flow were obtained with quadruple scans of the same plane with ECG trigger and breath holding; T₂-weighted image, phase encode (x-axis), read out (y-axis), and slice selection (z-axis).

III. RESULTS

A. Echo-dynamography

Three normal volunteers were examined by EDG and PC-MRA. Fig. 2a shows the conventional color Doppler

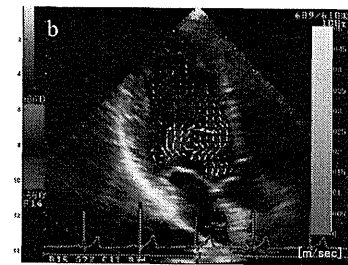
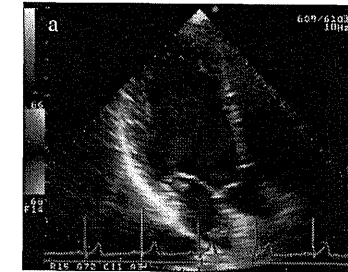


Fig. 2 a: conventional color Doppler, b: 2D distribution of blood flow vector obtained by echo-dynamography

echocardiography and Fig. 2b shows the 2D distribution of blood flow vector in LV at isovolumic contraction (IC) phase. The direction of the vector is indicated by arrow and the magnitude of the vector is indicated by the color scale.

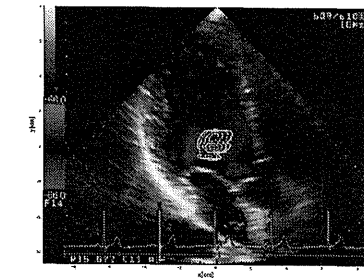


Fig. 3 Vortex flow presentation in echo-dynamography

Vortex component of the flow is represented in Fig. 3. The interval of the stream line shows the blood flow volume of 10 cm/s. The flow volume at the center of vortex was defined as vortex flow volume. At IC phase, a vortex is observed in the basal portion.

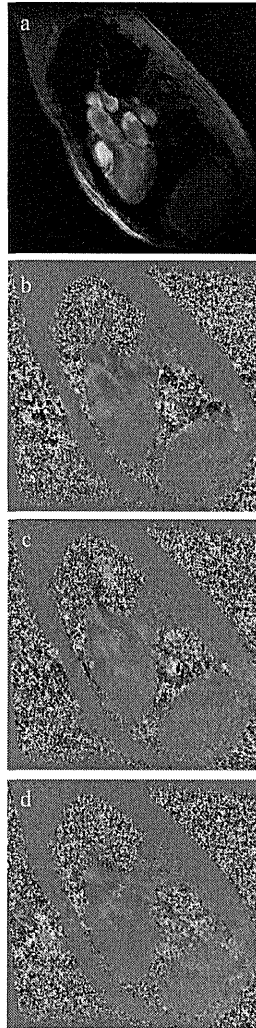


Fig. 4 PCMR images of normal heart.
 a: T₂-weighted image, b: PCMR encoded in slice select (SS),
 c: PCMR encoded in read out (RO),
 d: PCMR encoded in phase encode (PE)

B. Phase Contrast Magnetic Resonance Angiography

Fig. 4 shows the original Three-chamber view images acquired by PCMR. Fig. 4a shows T₂-weighted image and phase contrast image obtained simultaneously; Fig. 4b is encoded in slice select (SS) direction, Fig. 4c is encoded in read out (RO) direction, and Fig. 4d is encoded in phase encode (PE) direction respectively. These three phase contrast images were combined to figure out the vector flow map, and superimposed on the T₂-weighted image.



Fig. 5 2D distribution of blood flow vector obtained by PCMR

Fig. 5 shows the blood flow vector component on the scan plane at IC showing similar patterns with Fig. 2b. Originally, the velocity information acquired by conventional color Doppler method is only the velocity component along the ultrasonic beam. When deducing 2D distribution of blood flow vector from one-dimensional information, the vortex flow components tangential to the ultrasonic beam are found using stream function on the assumption that the velocity components perpendicular to the scan plane are zero. This is the fateful limitation of EDG in estimating vortex flow component from the view point of fluid dynamics. However, the result showed no contradiction with the fluid dynamics.

C. Vortex Flow in LV

The flow volume at the center of vortex was defined as vortex flow volume. The maximum value of the vortex flow from the closure of mitral valve to the opening of aortic valve was defined as isovolumic contraction (IC) vortex flow. These values were compared with LV inflow in normal (n=10) and DCM (n=13). IC vortex flow showed a strong correlation with maximum amplitude of A wave ($R^2=0.6097$, Fig. 6). The results indicate that LV inflow strongly affects LV vortex formation.

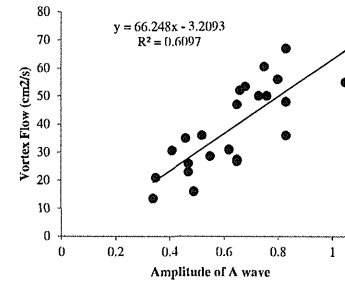


Fig. 6 Relation between atrial filling velocity and vortex flow

IV. DISCUSSION

EDG is superior in the spatial resolution in regards to the slice thickness. The slice thickness of the PCMR data was 8-mm in order to gain the signal-to-noise-ratio. Because the color Doppler contains the instantaneous velocity information, EDG is superior in temporal resolution, too. On the other hand, concerning reproducibility and a degree of freedom of dimensions, PC-MRA is superior to EDG.

The intraventricular vortex had close relationship with the maximum velocity of the A wave. The inertial force of the LV inflow continuing after mitral valve closure should be the origin of the LV vortex formation.

Our previous study [5] has shown that the size of the vortex became larger in failure heart compared with normal heart. The phenomenon was discussed with LV contraction and geometry. The results of the present study clearly showed that LV inflow also influence the size and location of LV vortex. When the heart rate is increased, LV inflow velocity is increased because of fusion of E and A waves. In such cases, large vortex at IC was observed. In cases of atrial fibrillation, LV vortex was not affected by A wave but the influence of E wave remained until IC.

Conventionally, diastole is occurred by releasing elastic energy stored by the preceding systolic deformation. This concept of systolic-diastolic coupling was discussed based on the physiology of contraction of the myocytes. In the present study, systolic-diastolic coupling was discussed based on LV blood flow such as vortex formation. Watanabe et al. found that the physiological flow path did not have an energy-saving effect by their multiscale, multiphysics heart simulator [7]. However, the vortex at early systole was affected by diastolic blood flow. Steen and Steen reported that the flow propagation velocity was originated by the movement of LV vortex [8]. The "vortex" in their report should be the "separation vortex" while our measurements included both "separation and rotating vortices". The difference should be discussed later.

V. CONCLUSIONS

In the present study, 3D blood flow vector using the PCMR was obtained and its 2D velocity components on the observed plane were compared with the 2D distribution of blood flow vector obtained by EDG method. In many cases, the vector components showed similar patterns in both methods.

REFERENCES

- [1] Aurigemma GP, and Gaasch WH. Diastolic Heart Failure. *N Engl J Med.* 2004; 351:1097-1105.
- [2] Ohtsuki, S. and M. Tanaka. The flow velocity distribution from the Doppler information on a plane in three-dimensional flow. *Journal of Visualization.* 2006; 9(1):69-82.
- [3] Tanaka M, Sakamoto T, Sugawara S, Nakajima H, Katahira Y, Ohtsuki S, Kanai H., Blood flow structure and dynamics, and ejection mechanism in the left ventricle: analysis using echo-dynamography. *J Cardiol.* 2008; 52(2): 86-101.
- [4] Tanaka M, Sakamoto T, Sugawara S, Nakajima H, Kaneyama T, Tabuchi H, Kanhira Y, Ohtsuki S, Kanai H., Physiological basis and clinical significance of left ventricular suction studied using echo-dynamography. *J Cardiol.* 2011; 58(3):232-44.
- [5] Nakajima H, Sugawara S, Kaneyama T, Tabuchi H, Ohtsuki S, Tanaka M, Saijo Y. Location of flow axis line in the left ventricle and its interaction with local myocardial motion. *J Echocardiogr.* 2011; 9(1): 24-27.
- [6] Uejima T, Koike A, Sawada H, Aizawa T, Ohtsuki S, Tanaka M, Furukawa T, Fraser AG. A new echocardiographic method for identifying vortex flow in the left ventricle: numerical validation. *Ultrasound Med Biol.* 2010; 36(5): 772-788.
- [7] Watanabe H, Sugimura S, Hisada T. The looped heart does not save energy by maintaining the momentum of blood flowing in the ventricle. *Am J Physiol Heart Circ Physiol.* 2008; 294(5):H2191-6.
- [8] Steen T and Steen S. Filling of a model left ventricle studied by colour M mode Doppler. *Cardiovasc Res.* 1994; 28(12):1821-7.

Mouse Model of Lymph Node Metastasis via Afferent Lymphatic Vessels for Development of Imaging Modalities

Li Li^{1,2}, Shiro Mori³, Maya Sakamoto⁴, Shoki Takahashi², Tetsuya Kodama^{1*}

1 Department of Biomedical Engineering, Graduate School of Biomedical Engineering, Tohoku University, Sendai, Japan, **2** Department of Diagnostic Radiology, Graduate School of Medicine, Tohoku University, Sendai, Japan, **3** Department of Oral and Maxillofacial Surgery, Tohoku University Hospital, Sendai, Japan, **4** Department of Oral Diagnosis, Graduate School of Dentistry, Tohoku University, Sendai, Japan

Abstract

Animal studies of lymph node metastasis are constrained by limitations in the techniques available for noninvasive monitoring of the progression of lymph node metastasis, as well as difficulties in the establishment of appropriate animal models. To overcome these challenges, this study has developed a mouse model of inter-lymph-node metastasis via afferent lymphatic vessels for use in the development of imaging modalities. We used 14- to 18-week-old MRL(Mp)-*lpr/lpr* (MRL/lpr) mice exhibiting remarkable systemic lymphadenopathy, with proper axillary lymph nodes (proper-ALNs) and subiliac lymph nodes (SILNs) that are 6 to 12 mm in diameter (similar in size to human lymph nodes). When KM-Luc/GFP malignant fibrous histiocytoma-like cells stably expressing the firefly luciferase gene were injected into the SILN, metastasis could be detected in the proper-ALN within 3 to 9 days, using *in vivo* bioluminescence imaging. The metastasis route was found to be via the afferent lymphatic vessels of the SILN, and metastasis incidence depended on the number of cells injected, the injection duration and the SILN volume. Three-dimensional contrast-enhanced high-frequency ultrasound imaging showed that the blood vessel volume and density in the metastasized proper-ALN significantly increased at 14 days after tumor cell inoculation into the SILN. The present metastasis model, with lymph nodes similar in size to those of humans, has potential use in the development of ultrasound imaging with high-precision and high-sensitivity as well as other imaging modalities for the detection of blood vessels in lymph nodes during the progression of metastasis.

Citation: Li L, Mori S, Sakamoto M, Takahashi S, Kodama T (2013) Mouse Model of Lymph Node Metastasis via Afferent Lymphatic Vessels for Development of Imaging Modalities. PLOS ONE 8(2): e55797. doi:10.1371/journal.pone.0055797

Editor: Kazuki Takabe, Virginia Commonwealth University School of Medicine, United States of America

Received: June 15, 2012; **Accepted:** January 2, 2013; **Published:** February 6, 2013

Copyright: © 2013 Li et al. This is an open-access article distributed under the terms of the Creative Commons Attribution License, which permits unrestricted use, distribution, and reproduction in any medium, provided the original author and source are credited.

Funding: The following funders had no role in study design, data collection and analysis, decision to publish, or preparation of the manuscript. <http://www.jpss.go.jp/english/e-grants/grants01.html> Grant-in-Aid for Scientific Research (B) (22390378) Grant-in-Aid for Challenging Exploratory Research (24659884) Grant-in-Aid for Scientific Research (B) (21390500) Grant-in-Aid for Challenging Exploratory Research (24659834) Grant-in-Aid for Scientific Research (B) (23300183) Grant-in-Aid for Challenging Exploratory Research (24650286)

Competing Interests: The authors have declared that no competing interests exist.

* E-mail: kodama@bme.tohoku.ac.jp

Introduction

Human lymph nodes are round or kidney-shaped organs of the immune system, 2 to 20 mm in diameter, that are distributed throughout the body [1,2]. Metastasis to regional lymph nodes is an important step in the dissemination of cancer [3], and often occurs at a relatively early stage of tumor development compared with distant metastasis, such as that to the liver and lung [4]. Accurate evaluation of lymph-node metastasis would be very helpful both for tumor staging and for formulation of the most appropriate treatment [5]. Despite the importance of nodal status for many solid malignancies, the methods available to assess lymph nodes are suboptimal [6]. Animal studies of lymph node metastasis are constrained by limitations in the techniques available for noninvasive monitoring of the progression of lymph node metastasis, as well as difficulties in the establishment of appropriate animal models [7].

The two major transplantation models of metastasis currently used are referred to as the spontaneous and the experimental metastasis models [8]. In the former model, tumor cells are injected into an anatomic location (orthotopic implantation), in the

tissue from which the tumor had been derived (orthotopic implantation) or in subcutaneous tissue (heterotopic implantation) [8]. In the latter model, tumor cells are directly injected into the circulation (e.g., into the spleen, tail vein or left cardiac ventricle), offering an attractive platform for the study of diagnostic imaging and treatment monitoring [9,10]. Most lymph node metastasis models are based on the spontaneous metastasis model [11], and these have provided valuable information concerning the biology of lymphatic metastasis [12,13], lymphatic architecture mapping [14,15], tumor-cell shedding and trafficking in lymphatic channels [16], and sentinel lymph node mapping [6,17,18].

However, the spontaneous metastasis model is limited by its poor performance for the dynamic quantitative assessment of the progression of lymph node metastasis using non-invasive approaches. This is maybe because both the latency period and the initial site of the metastasis vary considerably, and also because conventional imaging modalities are unable to identify changes in the internal structure of lymph nodes, of conventional mice, with a diameter of 1–2 mm [7,11,19].

This study describes the development of a mouse model of lymph node metastasis via the afferent lymphatic vessels, which is

suitable for use in the development of imaging modalities for dynamic quantitative assessment of metastatic progression. We used MRL/lpr mice developing systemic lymphadenopathy within 3 to 4 months of birth [20], with subiliac lymph nodes (SILNs) and proper axillary lymph nodes (proper-ALNs) that are 6 to 12 mm in diameter (similar in size to human lymph nodes). The extent of the metastasis to the proper-ALNs after injection of luciferase-expressing tumor cells into the SILN was evaluated using *in vivo* bioluminescence imaging and three-dimensional contrast-enhanced high frequency ultrasound imaging.

Materials and Methods

All *in vivo* studies were carried out in strict accordance with the recommendations in the Guide for Proper Conduct of Animal Experiment and Related Activities in Academic Research and Technology, 2006. The protocol was approved by the Institutional Animal Care and Use Committee of Tohoku University (Permit Number: 2010Be.LMO-76-20-255, 2009Be.A-6, 2010Be.A-7). All surgery was performed under sodium pentobarbital anesthesia, and all efforts were made to minimize animal suffering.

Cell Culture

KM-Luc/GFP cells, which stably express a fusion of the luciferase (Luc) and enhanced-green fluorescent protein (EGFP) genes, were prepared by transfection of MRL(Mp)Tr-*gld/gld* malignant fibrous histiocytoma-like (MRL(N-1) cells [21] (obtained from M. Ono, Tohoku University, on January 24, 2007), using pEGFP-Luc (BD Biosciences, Franklin Lakes, NJ, USA) and Lipofectin Transfection Reagent (Invitrogen, Carlsbad, CA, USA). MRL(N-1) cells were established from the spleen of an MRL/gld mouse [22]. We confirmed that KM-Luc/GFP cells have characteristics of malignant fibrous histiocytoma-like cells using histopathologic assessment: there was aggressive growth of pleomorphic fibro-histiocytic cells, with numerous mitotic figures and a storiform pattern (see Suppl. Fig. S1). KM-Luc/GFP cells were cultured in Dulbecco's Modified Eagle Medium (DMEM) supplemented with 10% fetal bovine serum (FBS) containing 1% L-glutamine-penicillin-streptomycin (Sigma-Aldrich, Tokyo, Japan) and 1% Geneticin G418 (Wako Pure Chemical Industries, Ltd., Tokyo, Japan). Before conducting the metastasis experiments, the absence of mycoplasma contamination in the cell cultures was ensured by testing with a mycoplasma detection kit (R&D Systems Inc., Minneapolis, MN, USA).

Mice

MRL/lpr mice, which develop systemic lymphadenopathy [20,23], were purchased from the Jackson Laboratory (Bar Harbor, ME, USA) and subsequently bred and maintained at the Institute for Animal Experimentation, Graduate School of Medicine, Tohoku University, Japan. Fifty-eight of these mice (weight, 35 to 45 g; age, 14 to 18 wk) were later used in the experiments. The mean longitudinal diameters of the SILN and proper-ALN of the mice, as measured using a digital caliper, were 8.4 ± 1.9 mm (mean \pm SD; $n = 55$) and 8.3 ± 1.7 mm (mean \pm SD; $n = 7$), respectively. Of these 58 mice, 42 were used for imaging of metastatic lymph nodes and as negative controls, and 16 were used for detection of the metastatic route.

Detection of Lymph Node Metastasis

The metastasis model was developed by injecting KM-Luc/GFP cells, suspended in 30 μ L PBS, into the SILN as follows: Group 1: 1×10^4 cells injected in 1 min ($n = 4$); Group 2: 5×10^4 cells injected in 1 min ($n = 4$); Group 3: 1×10^5 cells

injected in 1 min ($n = 4$); Group 4: 1×10^5 cells injected in 2 min ($n = 6$); and Group 5: 1×10^5 cells injected in 3 min ($n = 21$). PBS (30 μ L) was injected into the SILN as a negative control (Group 6; $n = 3$). Metastasis to proper-ALNs was analyzed using an *in vivo* bioluminescence imaging system (IVIS; Xenogen, Alameda, CA, USA) [24]. Before intraperitoneal injection of luciferin (150 mg/kg; Promega Co., Madison, WI, USA), each mouse was anesthetized with 2% isoflurane (Abbott Japan Co., Ltd., Tokyo, Japan) using an inhalation gas anesthesia system for small laboratory animals. On days 0, 3, 6, 9 and 14 post-inoculation (with the day of inoculation defined as day 0), luciferase bioluminescence was measured (10 min after luciferin injection) for 30 s using the IVIS.

Identification of Metastasis by *ex vivo* Bioluminescence Imaging

On day 14 post-injection of KM-Luc/GFP cells, luciferin was intraperitoneally injected into each mouse, and 10 min later, the mice were sacrificed by ether inhalation. The ALNs (proper and accessory) and SILN were surgically removed, and immediately placed in 6-well plates. Bioluminescence was then quantified for 30 s using the IVIS.

Histological Evaluation

Following *ex vivo* observation of bioluminescence, harvested lymph nodes were fixed overnight in 18.5% formaldehyde in phosphate-buffered solution (PBS), dehydrated, and embedded in paraffin. The embedded specimens were cut into 4- μ m-thick serial sections and either stained with hematoxylin and eosin (H&E), or immunostained for luciferase after antigen retrieval. For the latter procedure, sections were incubated for 10 min at 37°C with 0.1% trypsin in Tris buffer, and blocked with 10% rabbit serum (Nichirei Biosciences Inc., Los Angeles, CA, USA) for 10 min at room temperature (RT) to reduce non-specific protein binding. To detect luciferase protein, sections were incubated overnight at 4°C with a goat polyclonal anti-luciferase antibody (ab81823; 1:1000; Abcam plc, Tokyo, Japan). Immunoreactivity was detected using biotinylated polyclonal rabbit anti-goat immunoglobulin (1:800; Dako Japan Inc., Tokyo, Japan) for 30 min at RT, peroxidase-conjugated streptavidin (Nichirei Bioscience Inc.) for 30 min at RT, and diaminobenzidine (DAB) as a chromogen in accordance with the manufacturer's protocol.

Detection of Luciferase Activity in Organs by Luminometry

To determine luciferase activity in the organs post-inoculation, the inoculated SILN, the ipsilateral proper- and accessory-ALNs, ipsilateral mandibular lymph node, ipsilateral lumbar aortic lymph node, caudal mesenteric lymph node, contralateral proper-ALN, contralateral SILN, liver and lungs were surgically removed on day 14 post-inoculation of KM-Luc/GFP cells (Group 3; $n = 4$) or PBS (Group 6; $n = 3$). Tissues were weighed, frozen in liquid nitrogen, homogenized with reporter lysis buffer (Promega Co.), and centrifuged at 12,000 \times g for 2 min at 4°C. Supernatant samples (10 μ L each) were examined for luciferase activity using 50 μ L luciferase assay reagent containing D-Luciferin (Promega Co.). Bioluminescence was measured at RT for 10 s using a luminometer (TD-20/20; Turner BioSystems, Sunnyvale, CA, USA). Results are presented in arbitrary units (AUs).

Visualization of the Metastatic Route

After anesthetization via intraperitoneal injection of 5% sodium pentobarbital (40 mg/kg; $n = 15$), visualization of the metastatic

route was performed using at least 1 of 3 imaging systems: an *in vivo* fluorescence imaging system (IVIS; $n = 1$); an infrared photodynamic camera (PDE; Hamamatsu Photonics K.K., Hamamatsu, Japan; $n = 12$); or a high-speed fluorescence video camera system (HS-FVCS; $n = 2$) comprising a high-power xenon light source (MAX-301; Asahi Spectra Co., Ltd., Tokyo, Japan) and a charge coupled device (CCD) camera (HAS-220; Ditect, Tokyo, Japan) with a lens (NL-Z07545HR; Moritex Co., Tokyo, Japan). The IVIS emitted and detected light at wavelengths of 710 to 760 nm and 810 to 875 nm, respectively, whereas the PDE emitted light at 760 nm and detected light at wavelengths greater than 820 nm. After injection of indocyanine green (ICG; excitation wavelength, 805 nm; emission wavelength, 840 nm; Daiichi Sankyo, Tokyo, Japan) [25] into the SiLN, the IVIS and PDE were used to detect ICG flow in afferent lymphatic vessels from the SiLN to the proper-ALN. A total of 30 μ L ICG (125 μ g/mL) was injected at speeds of 0.6 mL/h (IVIS, $n = 1$) or 0.5 to 3.0 mL/h (PDE, $n = 12$), using an infusion pump (KDS100; KD Scientific Inc., Holliston, MA). After the PDE had been used to investigate the effect of injection speed into the SiLN on the incidence of metastasis to the proper-ALN (with injection speeds ranging from 0.5 to 1.0, and 3.0 mL/h; $n = 4$ per group), the HS-FVCS was used to determine whether metastasis from the SiLN to the proper-ALN had occurred via the veins or the afferent lymphatic vessels ($n = 2$). Under anesthesia, an arc-shaped incision was made in the abdominal skin from the subiliac to the proper axillary region, and 30 μ L of 1.8 μ g/ μ L fluorescein isothiocyanate-labeled bovine serum albumin (FITC-BSA; MW, 70,000; excitation wavelength, 488 nm; emission wavelength, 518 nm; Sigma-Aldrich) was then injected into the SiLN at 1.0 mL/h by means of an infusion pump. A high-power xenon light source with an appropriate filter (MX0490; Asahi Spectra Co., Ltd.) was used to deliver excitation light at a wavelength of 490 \pm 2 nm, and a CCD camera with an appropriate filter (MX0510; Asahi Spectra Co., Ltd.) was employed to detect light at a wavelength of 510 \pm 2 nm.

To confirm the route of metastasis histologically ($n = 1$), 30 μ L Indian ink was injected into the SiLN, and 10 min later, the skin from the subiliac to the proper axillary region, including the veins and afferent lymphatic vessels, was surgically removed and dissected, and the tissue stained with H&E to observe the cross-sectional surface.

Preparation of Acoustic Liposomes

Acoustic liposomes (ALs) were used as ultrasound contrast agents, and were prepared as described previously [26]. The number of ALs in the lipid solution was calculated to be 3.3×10^{12} bubbles/mL [27]. The peak diameter of the number distribution was 0.20 ± 0.08 μ m, and the zeta potential was -2.40 ± 0.51 mV. Approximately 20% of the ALs contained both liquid and gas, whereas approximately 80% contained liquid alone (i.e., were non-acoustic) [27].

3D Reconstruction of the Intranodal Microvasculature in Proper-ALNs using Contrast-enhanced High-frequency Ultrasound with ALs

To reveal changes in the angiogenic vessel density within the metastasized proper-ALNs, contrast-enhanced high frequency ultrasound (CE-HFUS) with ALs was used. Subsequent to injection of the SiLN, over a 1 min period, with either 1×10^5 KM-Luc/GFP cells in 30 μ L PBS (Group 3; $n = 4$) or PBS only (Group 6; $n = 3$), metastasis to the proper-ALN was confirmed by bioluminescence imaging on days 0, 9 and 14. On the same days, a 3D vascular image of the proper-ALN was

reconstructed using ALs and a high-frequency ultrasound imaging system (HFUS; VEVO770; VisualSonics, Toronto, Canada) with a 35-MHz center-frequency transducer (RMV-703; axial resolution, 50 μ m; focal length, 10 mm) at 100% transmittance power. Mice anesthetized with 2% isoflurane were placed on a stage maintained at 38°C (TM150, VisualSonics) during the scanning period. An ultrasound transmission gel (Parker Laboratories, Inc., Fairfield, NJ, USA) was placed on the proper-ALN, the focal length of the transducer adjusted using a stage control system (Mark-204-MS, Sigma Koki Co., Ltd., Tokyo, Japan), and the working distance of the scan determined by moving the transducer over the proper-ALN using the stage control system.

Generating a 3D dataset requires assessment of multiple 2D ultrasound images that are then reconstructed to achieve the desired 3D image. In our previous experiments [28], we found that the half-life of ALs in solid tumors was 84 ± 12 s when a 100 μ L bolus (lipid concentration, 1 mg/mL) was injected manually into the caudal veins of mice within a 10 s period ($n = 4$) [29]. To extend the lifespan of ALs and achieve a longer diagnostic window in the current study, a 200 μ L bolus of ALs was injected manually into the caudal vein of each MRL/lpr mouse over a 40 s period, which resulted in an *in vivo* AL half-life of 284 ± 13 s (mean \pm SEM; $n = 3$; data not shown). Multiple 2D images of the proper-ALNs were then captured over a period of 156 ± 12 s (mean \pm SEM; $n = 7$), shorter than that of the *in vivo* half-life of the ALs, and blending algorithms were used to convert these 2D slices into 3D volumetric images. Blood vessel structures were mapped and reconstructed by tracking the flow of ALs through the vessels, using the software provided with the VEVO 770 system. Regions of interest were drawn manually on every 2D image along the lymph node margins. The blood vessel volumes and densities within the proper-ALNs were calculated using VEVO770 contrast-mode software. Extracted 2D slices were obtained for analysis at 61 ± 5 s (mean \pm SEM; $n = 7$).

Statistical Analyses

All measurements are presented as either the mean \pm SD or mean \pm SEM. Differences between groups were determined by two-way ANOVA followed by the Tukey-Kramer test. Correlations between *in vivo* and *ex vivo* bioluminescence results were determined using Spearman's rank correlation coefficient test. Comparisons of metastasis incidence between the various inoculation conditions were performed using Fisher's exact probability test. A *P* value less than 0.05 was considered to be an indication of statistical significance. Statistical analyses were performed using Excel 2007 (Microsoft, USA) with Statcel2 software.

Results

Metastatic Flow and Route

To identify the metastatic route from the SiLN to the proper-ALN, ICG was injected into the SiLN at 0.5 to 3.0 mL/h (using a syringe pump), and the flow was observed with the IVIS (Fig. 1A) and PDE (Fig. 1B). The ICG flowed via a superficial route at a speed of 0.26 to 2.09 mm/s (Fig. 1C) and accumulated in the proper-ALN of all mice, independent of the injection speed. Flow speed was calculated by dividing the distance, *l*, by the duration of time that had elapsed post-injection (see Supplementary Video S1 and Fig. 1B). Next, the route to the proper-ALN in the abdominal skin flap was investigated (Fig. 1D). To determine whether metastasis had occurred via the veins or the afferent lymphatic vessels, FITC solution was injected into the SiLN and the flow observed using HS-FVCS (Fig. 1D). A thick, superficial epigastric vein was identified under visible light (Fig. 1D*b*), while the route

filled with FITC-BSA solution was identified by fluorescence imaging to be a distance of 200 μ m from the vein (Fig. 1D*c*). To confirm that this route involved flow via the afferent lymphatic vessels, Indian ink was injected into the SiLN. H&E staining demonstrated that the Indian ink flowed via the afferent lymphatic vessels that connected the SiLN to the proper-ALN (Fig. 1D*d*).

Metastasis in the Lymph Node

Using IVIS, *in vivo* bioluminescence signals were detected in the ALNs within 3 to 9 days, but were not evident in other organs until day 14 (Fig. 2Aa). *Ex vivo* bioluminescence signals were detected in the proper-ALNs (Fig. 2Ab), but not in the accessory-ALNs (data not shown). A significant relationship was identified between the *in vivo* and *ex vivo* bioluminescence signals (correlation coefficient

[r] = 0.9161, $P = 0.0023$, $n = 12$; Fig. 2B). These results indicate that the *in vivo* bioluminescence signals monitored in the axillary region had been emitted only by the proper-ALNs. H&E and immunohistochemical staining of the excised SiLN and proper-ALN specimens confirmed that the large tumor mass within the SiLN was composed of implanted KM-Luc/GFP cells, and that a metastatic tumor was located in the marginal region of the proper-ALN (Fig. 2C). To further investigate the extent of the systemic metastasis, the luciferase activities in selected organs were measured on day 14 ($n = 4$; Fig. 2D). The results showed that metastases had developed primarily in the proper-ALN and to a lesser degree in the adjacent mandibular lymph node, but not significant in the accessory-ALN or other distant lymph nodes. A small number of cells were also detected in the liver and lungs.

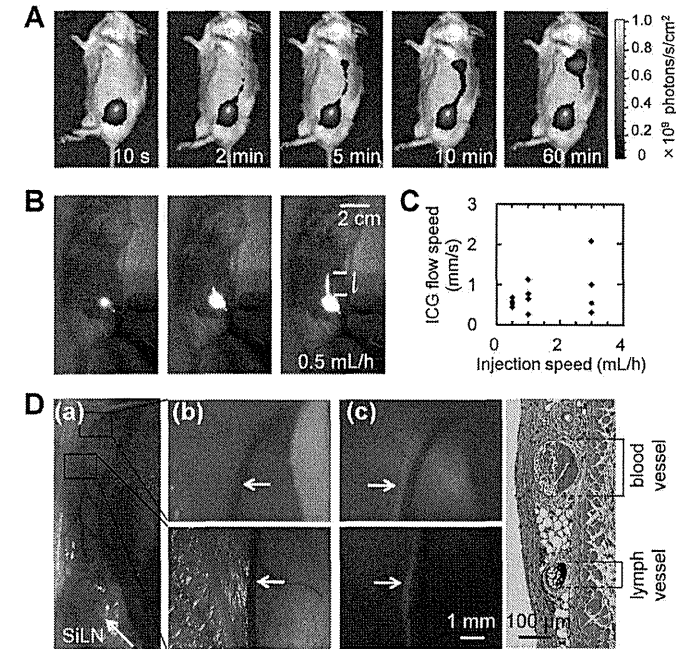


Figure 1. Metastatic flow and route. A. ICG flow from the SiLN to the proper-ALN, observed using an *in vivo* fluorescence imaging system (IVIS; $n = 1$). B. Representative PDE images, following an ICG injection speed of 0.5 mL/h. The speed of ICG flow was calculated by dividing the distance, *l*, by the duration of time that had elapsed post-injection. C. Graph of the relationship between ICG flow speed and intra-SiLN injection speed (low, 0.5; medium, 1.0; high, 3.0 mL/h; $n = 4$ per group), revealing a low level of variation between individual experiments in the low-speed group. D. HS-FVCS image of the afferent lymphatic vessels after intra-SiLN injection of FITC-BSA solution ($n = 2$). (a) Area near the SiLN and proper-ALN captured by a normal digital camera. Two regions of interest were selected. (b) Bright field images obtained by HS-FVCS, without use of a fluorescence filter. A thick superficial epigastric vein (→) was observed. (c) Fluorescence images obtained by HS-FVCS, with use of an appropriate fluorescence filter (bandwidth: 510 \pm 2 nm). A new flow channel filled with FITC-BSA solution (→) appeared at a distance of about 200 μ m from the vein. (d) Results of hematoxylin and eosin (H&E) staining. The flow channel was identified as the afferent lymphatic vessels by injection of Indian ink. The vein was not stained ($n = 1$). doi:10.1371/journal.pone.0055797.g001

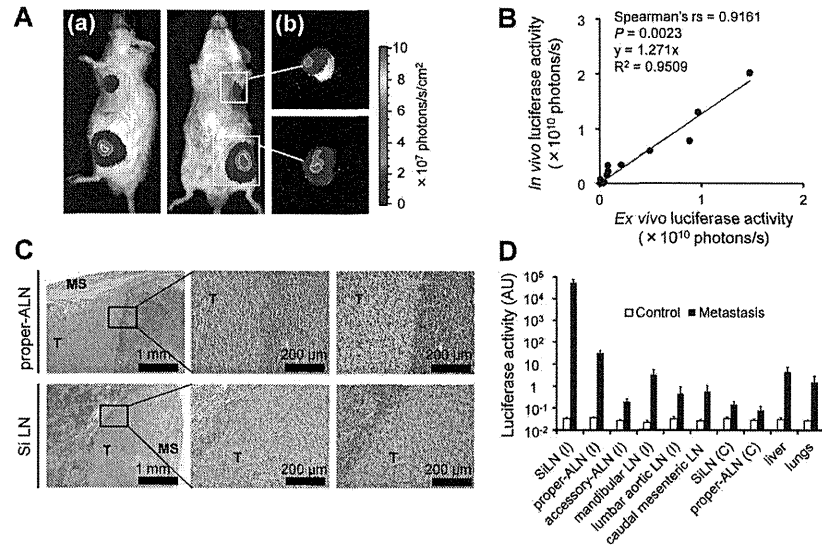


Figure 2. Establishment of the model of lymph node metastasis. A. Representative images captured by *in vivo* bioluminescence imaging of a mouse with tumor cells grafted into the SiLN to promote metastasis to the ALN. (a) *In vivo* and (b) *ex vivo* bioluminescence signals in the proper-ALN and SiLN on day 14 post-inoculation, indicating that the proper-ALN is the draining lymph node. B. Graph showing the high correlation between *in vivo* and *ex vivo* bioluminescence ($P=0.0023$; Spearman's rank correlation coefficient (r_s) = 0.9161; SiLN, $n=6$; proper-ALN, $n=6$). C. Results of histological verification. Tumor cells stained with H&E and luciferase-positive immunohistochemical signals in the proper-ALN and SiLN. MS: marginal sinus. T: tumor. D. Dissemination of KM-Luc/GFP cells (metastasis, $n=4$) or PBS alone (control, $n=3$) to each organ, assessed on day 14 post-injection of the SiLN. I, ipsilateral; C, contralateral; LN, lymph node. Error bars indicate the SEM values. doi:10.1371/journal.pone.0055797.g002

When PBS alone was injected as a control ($n=3$), the luciferase activity was found to be at background levels.

Factors Associated with Metastasis

In the current model, cells metastasized from the SiLN to the proper-ALN. To test the hypothesis that the primary parameters related to metastasis are the number of cells injected, the injection duration and the SiLN volume, the effect of each parameter on metastasis was investigated in mice with SiLNs 6 to 12 mm in longitudinal diameter (Fig. 3A). When the injection duration was held constant (1 min), metastatic incidence was found to increase with the number of cells injected (from 1×10^4 to 1×10^5 cells), with all 4 mice examined exhibiting metastasis (an incidence of 100%) upon injection of 1×10^5 cells (Fig. 3Aa). In contrast, metastatic incidence was found to decrease with an increase in the SiLN volume, when the number of cells (1×10^5) and injection duration (3 min) were held constant. Specifically, the incidence of metastasis was found to be 100% at SiLN volumes less than 100 mm^3 , but significantly reduced at volumes greater than 150 mm^3 (Fig. 3Ac).

Although the relationship between metastasis incidence and injection duration (1, 2 or 3 min) was found to be not statistically significant, there appeared to be a tendency toward greater metastasis with injections of shorter duration (Fig. 3Ab). To

consider the effect of all 3 parameters on metastatic incidence, the new parameter of cells $\text{mm}^{-3} \text{ min}^{-1}$ was introduced; this parameter is directly proportional to the injected cell number and metastasis incidence, while inversely proportional to the injection duration and SiLN volume. It was found that a cells $\text{mm}^{-3} \text{ min}^{-1}$ value greater than 4.72×10^2 resulted in 100% metastasis induction ($n=39$; Fig. 3B).

Progression of Metastasis Assessed using CE-HFUS with ALs

CE-HFUS enables real-time reconstruction of co-registered sections into a 3D image that reflects tumor vascularity [28,30]. Based on this ability, it was hypothesized that CE-HFUS would be suitable for the analysis of cancer progression, and thus could be used to determine whether the proposed mouse model is an appropriate model for the development of diagnostic imaging modalities for lymph node metastasis. Qualitative and quantitative investigations of blood vessel volumes and densities within the metastatic lymph nodes were carried out using CE-HFUS with ALs on days 0, 9 and 14, and the findings were compared with those of the negative control (PBS injection only) group (Fig. 4, A and B). The images were captured within $156 \pm 12 \text{ s}$ (mean \pm SEM; $n=7$) a time period shorter than the *in vivo* half-life of the ALs ($284 \pm 13 \text{ s}$; mean \pm SEM;

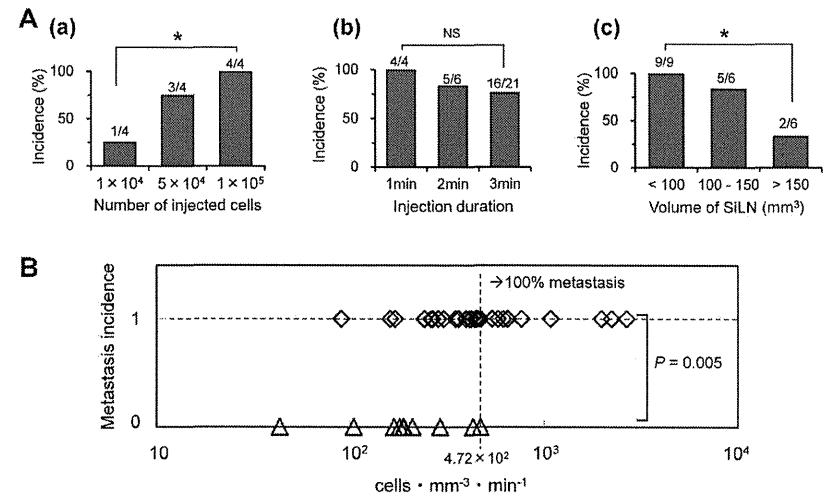


Figure 3. Parameters related to the incidence of metastasis. A. Effects of inoculation conditions on the incidence of lymph node metastasis. Metastatic incidence increased with injection of a larger number cells (a), did not vary significantly with injection duration (b), but decreased with a larger SiLN volume (c). In the values presented above the bars, the denominator represents the number of inoculated mice while the numerator represents the number of mice with metastases in the proper-ALN. NS indicates $P>0.05$; * $P<0.05$ calculated by Fisher's exact probability test. B. Assessment of the correlation between the above 3 parameters and metastasis incidence, using a new parameter, cells $\text{mm}^{-3} \text{ min}^{-1}$. When metastasis incidence was set at 1, 100% metastasis was achieved when the cells $\text{mm}^{-3} \text{ min}^{-1}$ value exceeded 4.72×10^2 ($n=39$). Analyses were performed with the Mann-Whitney U test. doi:10.1371/journal.pone.0055797.g003

$n=3$) (see Materials and Methods). The period of time over which the images were captured may therefore be sufficiently short to avoid detection of leakage of ALs from vasculature of the proper-ALNs [31]. 2D images extracted from the 3D reconstruction images of the blood vessels demonstrated localized, dense areas of neovasculature (arrows in the upper panels and dotted circles in the lower panels, Fig. 4A), and revealed their development over time. Although it was difficult to confirm that the imaged region was identical for each time point, obtaining 2D vascular-reconstruction images nonetheless enables identification of recognizable remodeling of the vasculature during tumor progression. Since the co-registered sections were not necessarily representative of the entire tumor due to tumor heterogeneity [32], the 3D blood vessel volumes and densities of the metastatic lymph nodes were subsequently investigated quantitatively (Fig. 4B). Values for blood vessel volume and density were normalized against those on day 0. Blood vessel volume significantly increased from 1.00 (day 0) to 1.07 ± 0.10 (day 9) and 1.36 ± 0.05 (day 14) ($P<0.05$); blood vessel density increased from 1.00 (day 0) to 1.01 ± 0.07 (day 9) and 1.24 ± 0.03 (day 14) ($P<0.05$). On day 14, both blood vessel volume ($P<0.05$) and blood vessel density ($P<0.01$) were significantly higher than in the negative control group.

Discussion

The present study has developed a novel model of lymph-node metastasis, based on the injection of KM-Luc/GFP cells into the

SiLNs of MRL/lpr mice [20] exhibiting remarkable systemic lymphadenopathy. The importance of this new model is that it is ideally suited for use in the development of imaging modalities to improve the assessment of cancer metastasis to lymph nodes. Mice carrying a lymphoproliferation (*lpr*) mutant gene have defects in the *Fas* gene [33] that result in spontaneous development of an autoimmune lupus syndrome characterized by autoantibody production and massive lymphoproliferation. In this study, the diameter of the lymph nodes was found to be between 6 and 12 mm, which is similar to that of human lymph nodes. The KM-Luc/GFP cell line is a type of transformed MRL/N-1 cell line [21] carrying the *gld* (generalized lymphoproliferative disease) gene, a missense mutation in the *Fas* ligand gene [34]. Since the *Fas*/*Fas* ligand axis is relevant to apoptosis [35], apoptosis may not be related to the mechanisms of metastasis in the present model.

The incidence of metastasis in the proper-ALN was found to depend on the number of cells injected, the injection duration and the SiLN volume, with complete (100%) metastasis achieved using cells $\text{mm}^{-3} \text{ min}^{-1}$ values greater than 4.72×10^2 (Fig. 3B). These findings indicate that increasing the number of cells injected per minute and the internal pressure within the SiLN enhances the efficiency of the formation and survival of cell colonies, resulting in an increase in metastatic incidence [16,36,37].

The American Joint Committee on Cancer (AJCC) classifies lymph node metastases on the basis of histological results; isolated tumor cells (cell clusters with diameters $\leq 0.2 \text{ mm}$), micrometas-

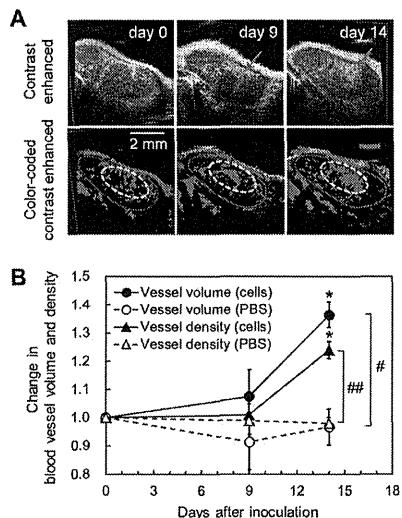


Figure 4. Monitoring of metastatic progression by CE-HFUS with ALNs. A. Imaging of the temporal changes in angiogenic vessel density in a cross-section of a metastatic proper-ALN, visualized by CE-HFUS with ALNs. Blood vessel density increased with tumor progression. Red circles indicate the proper-ALN boundary, arrows and dotted lines indicate the AL-enhanced region, and green highlighting indicates the dense area of neovascularity in the proper-ALN. B. Results of 3D quantitative analysis of the temporal changes in blood vessel volume and density in metastatic proper-ALNs. The term "cells" indicates the metastasized group (1×10^6 cells/min, $n=4$) and "PBS" the negative control group ($n=3$). Values for each group were normalized against the measurement on day 0. Error bars indicate the SEM values. * is for comparison of the temporal change within each group; # is for comparison between groups. * or #, $P < 0.05$; ** or ##, $P < 0.01$, calculated using two-way ANOVA followed by the Tukey-Kramer test. doi:10.1371/journal.pone.0055797.g004

tases ($0.2 \text{ mm} < \text{tumor cell clusters} \leq 2 \text{ mm}$) and macrometastases (tumor cell clusters $> 2 \text{ mm}$) [38]. Some studies have revealed a significant relationship between the presence of isolated tumor cells or micrometastases in lymph nodes and poorer prognosis [39,40], whereas others have failed to find such an association [41–43]. However, lymph node macrometastases larger than 2 mm (on the basis of cluster size) have been established to be of prognostic significance [39].

Currently, a lymph node size greater than 10 mm in the short-axis diameter, determined by CT and MRI, is considered to be the most important radiologic criterion for lymph node metastasis [44,45]. However, this size-based characterization of lymph node metastasis frequently leads to erroneous diagnosis, as when, for example, normally-sized lymph nodes are metastatic or, conversely, abnormally enlarged lymph nodes are solely the consequence of reactive swelling [46]. To improve diagnostic accuracy, it is vital that a new set of diagnostic criteria are established for lymph node

metastasis, based on the development and use of high-resolution imaging techniques and specific contrast agents.

As angiogenesis has been found to be an important marker of cancer progression [47], detection of changes in the structures of angiogenesis-induced blood vessels has become a key strategy for the diagnosis of cancer involvement [48]. Based on this finding, the changes in angiogenic vessel volume and density within the proper-ALN were examined using 2D/3D CE-HFUS with ALNs [28]. As shown in Fig. 4, significant increases in the angiogenic vessel volume and density in the proper-ALN, compared with the control, were evident at day 14, suggesting that the detection of angiogenesis could be an effective approach to detect lymph node metastasis. In addition, the angiogenesis occurred predominantly after the establishment of metastasis on day 14, and not by day 9. This suggests that angiogenesis may show a period of dormancy during the development of metastasis. Hanahan and Folkman [49] have proposed the concept of an "angiogenic switch" to describe the activation of angiogenesis during the development of a tumor. When a tumor has grown beyond approximately 1 to 2 mm^3 in volume, it cannot rely on the diffusion of metabolites to meet its needs and therefore must recruit and develop new vessels through the well-known process of angiogenesis [50]. The pattern of the increase in vascularity in the present model is similar to that previously reported [51]. Therefore, the model described here provides an excellent opportunity for the serial quantification and analysis of the changes in blood vessel structure in the lymph nodes, during the progression of metastasis, using non-invasive techniques.

The intravital imaging systems currently used in preclinical cancer research employ magnetic resonance imaging (MRI) at a resolution of 10 to 100 μm , X-ray computed tomography imaging (CT) at a resolution of 50 μm , ultrasound imaging at a resolution of 50 μm , and positron emission tomography at a resolution of 1 to 2 mm [52]. As the size of the mouse lymph node in the present model is similar to that of the human lymph node, the use of this metastasis model to investigate and develop these imaging systems would likely allow for the establishment of new diagnostic methods for diagnosis of metastasis, based on the dynamics of angiogenesis.

In conclusion, we have established a mouse model of inter-lymph node metastasis via afferent lymphatic vessels, using mice exhibiting remarkable systemic lymphadenopathy, with the proper-ALNs and SILNs 6 to 12 mm in diameter (similar in size to human lymph nodes). This model may be used for the development of highly functionalized, high-resolution ultrasound as well as other imaging modalities for the detection of blood vessels in lymph nodes during metastatic progression.

Supporting Information

Figure S1 Malignant fibrous histiocytoma (MFH)-like cells.

(TIFF)

Video S1 Visualization of the route of lymph node metastasis.

(AVI)

Acknowledgments

We thank M. Nose for discussion on the immunohistological analysis. We thank M. Ono for providing the MRL/N-1 cells, and also S. Horie, Y. Watanabe and N. Sax for their technical assistance.

Author Contributions

Conceived and designed the experiments: LL SM MS ST TK. Performed the experiments: LL. Analyzed the data: LL TK. Contributed reagents/materials/analysis tools: LL TK. Wrote the paper: LL TK.

References

- Roit I, Brostoff J, Male D (2001) Immunology. Edinburgh: Mosby.
- Warwick, Roger; Peter L Williams (1973) [1858]. Angiology. Chapter 6. Gray's anatomy, illustrated by Richard E. M. Moore (Thirtieth ed). London: Longman. p. 588–785.
- Ran S, Volk L, Hall K, Fister MJ (2010) Lymphangiogenesis and lymphatic metastasis in breast cancer. *Pathophysiology* 17: 229–251.
- Ito Y, Nakamichi H, Kodera Y, Hirai T, Nakao A, et al. (2010) Characterization of a novel lymph node metastasis model from human colonic cancer and its preclinical use for comparison of anti-metastatic efficacy between oral S-1 and UFTLV. *Cancer Sci* 101(10): 1853–1860.
- Lutman GV, Havrilesky LJ, Cragun JM, Secord AA, Caligiore B, et al. (2006) Pelvic lymph node count is an important prognostic variable for FIGO stage I and II endometrial carcinoma with high-risk histology. *Gynecol Oncol* 102: 92–97.
- Burton JB, Johnson M, Sato M, Koh SB, Mulholland DJ, et al. (2008) Adrenocorticotrophic hormone expression imaging to directly detect sentinel lymph node metastasis of prostate cancer. *Nat Med* 14: 882–888.
- Servais EL, Golouvs C, Bognard AJ, White J, Sadehmi M, et al. (2011) Animal models and molecular imaging tools to investigate lymph node metastases. *J Mol Med* 89: 753–769.
- Khanm M, Hunter K (2005) Modeling metastasis in vivo. *Carcinogenesis* 26: 513–523.
- Grohau KC, Wirtzfeld LA, MacKenzie LT, Poterack CO, Groom AC, et al. (2005) Three-dimensional high-frequency ultrasound imaging for longitudinal evaluation of liver metastases in preclinical models. *Cancer Res* 65: 5231–5237.
- Kanaya H, Kuruppu DK, Donahue JM, Choi EW, Kawasaki H, et al. (2005) Mouse models of subcutaneous splenic reservoir for multiple portal venous injections to treat liver malignancies. *Cancer Res* 65: 3023–3027.
- Nathanson SD (2007) Preclinical models of regional lymph node tumor metastasis. *Cancer Treat Res* 135: 129–156.
- Kozaki K, Miyaiishi O, Tsukamoto T, Tatematsu Y, Hida T, et al. (2000) Establishment and characterization of a human lung cancer cell line NCI-H460-LN135 with consistent lymphogenous metastasis via both subcutaneous and orthonasal propagation. *Cancer Res* 60: 2545–2549.
- Doki Y, Murakami K, Yamaura T, Sugiyama S, Mizuki T, et al. (1999) Metastatic lymph node metastasis model by orthotopic intrapulmonary implantation of Lewis lung carcinoma cells in mice. *Br J Cancer* 79: 1121–1126.
- Dietz M, Schubert R, Hinale P (2003) Blue liposomes for identification of the sentinel lymph nodes in pigs. *Lymphology* 36: 39–47.
- Soares EG, Kim S, Lawrence KC, DeCruz AM, Parung GP, et al. (2005) Intraoperative sentinel lymph node mapping of the lung using near-infrared fluorescent quantum dots. *Ann Thorac Surg* 79: 269–277; discussion 269–277.
- Hayashi K, Jiang P, Yamauchi K, Yamamoto N, Tsuchiya H, et al. (2007) Real-time imaging of tumor-cell shedding and trafficking in lymphatic channels. *Cancer Res* 67: 8224–8228.
- Huynh ST, Burton JB, Sato M, Carey M, Gambhir SS, et al. (2009) A potent, imaging adenosine vector driven by the cancer-selective mdr1 promoter that targets breast cancer metastases. *Clin Cancer Res* 15: 3120–3134.
- Swirski FK, Berger CR, Figueroa JL, Meupel TK, von Andrian UH, et al. (2007) A near-infrared cell tracker reagent for multicentric in vivo imaging and quantification of leukocyte immune responses. *PLoS One* 2: e1075.
- Bibby MC (2004) Orthotopic models of cancer for preclinical drug evaluation: advantages and disadvantages. *Eur J Cancer* 40: 852–857.
- Murphy ED, Roth JB (1978) Antigenicity and lymphoproliferation: induction by mutant gene lpr, and acceleration by a male-associated factor in strain BXSR mice; Rose N, Bigazzi P, Warner L, editors. New York: Elsevier/North-Holland. p. 207–221.
- Furukawa H, Kitazawa H, Kaneko I, Kikuchi K, Tshima S, et al. (2009) Mst1 cells inhibit CD8+ T cell-mediated rejection of a malignant fibrous histiocytoma-like tumor: Involvement of Fas-Fas ligand axis. *Am J Immunol* 5: 89–97.
- Hasegawa H, Kohno M, Sasaki M, Inoue A, Ito MK, et al. (2003) Antagonist of monocyte chemoattractant protein 1 ameliorates the initiation and progression of lupus nephritis and renal vasculitis in MRL/lpr mice. *Arthritis Rheum* 48: 2555–2566.
- Gyotoku Y, Abdelmassouh M, Speranza F, Lini S, Lambert PH (1987) Cryoglobulinemia induced by monoclonal immunoglobulin G rheumatoid factors derived from autoimmune MRL/MpJ-lpr/lpr mice. *J Immunol* 138: 3785–3792.
- Dickson FW, Hamner B, Ng CY, Hall MM, Zhou J, et al. (2007) In vivo bioluminescence imaging for early detection and monitoring of disease progression in a murine model of neuroblastoma. *J Pediatr Surg* 42: 1172–1179.
- Ueno N, Suzuki M, Yamamoto M, Inuzuka K, Sagara D, et al. (2009) Indocyanine green fluorescence angiography for intraoperative assessment of blood flow: a feasibility study. *Eur J Vasc Endovasc Surg* 35: 203–207.
- Kodama T, Tomita N, Horie S, Sax N, Iwasaki H, et al. (2010) Morphological study of acoustic liposomes using transmission electron microscopy. *J Electron Microscop* 9: 167–196.
- Kodama T, Aoi A, Watanabe Y, Horie S, Kodama M, et al. (2010) Evaluation of transection efficiency in skeletal muscle using nano/microbubbles and ultrasound. *Ultrasound Med Biol* 36: 1196–1205.
- Kodama T, Tomita N, Yagihara Y, Horie S, Funamoto K, et al. (2011) Volumetric and angiogenic evaluation of anti-tumor effects with acoustic liposome and high-frequency ultrasound. *Cancer Res* 71: 6957–6964.
- du Toit LG, Groender T, Pillay V, Choomara YE, Kumbana T (2011) Investigating the effect of polymeric approaches on circulation time and physical properties of nanobubbles. *Pharm Res* 28: 494–504.
- Loveless ME, Li X, Huananai J, Lytlechik A, Dwannt B, et al. (2008) A method for assessing the microvasculature in a murine tumor model using contrast-enhanced ultrasonography. *J Ultrasound Med* 27: 1699–1709.
- Motomura Y, Maehira H (2006) A new concept for micro/nanobubble therapeutics in cancer chemotherapy: mechanism of ultrasonic accumulation of proteins and the anti-tumor agent sodium. *Cancer Res* 46: 6387–6392.
- Kiessling F, Le-Huu M, Kunert T, Thorn M, Voelcker S, et al. (2009) Improved correlation of histological data with DCE-MRI parameter maps by 3D reconstruction and parameterization of the histological images. *Eur Radiol* 19: 1070–1086.
- Watanabe-Fukunaga R, Brannan CH, Copeland NG, Jenkins NA, Nagata S (1992) Lymphoproliferation disorder in mice explained by defects in Fas antigen that mediates apoptosis. *Nature* 356: 314–317.
- Takahashi T, Tsunaka M, Brannan CH, Jenkins NA, Copeland NG, et al. (1994) Generalized lymphoproliferative disease in mice, caused by a point mutation in the Fas ligand. *Cell* 76: 959–976.
- Nagata S (1994) Apoptosis regulated by a death factor and its receptor: Fas ligand and Fas. *Philos Trans R Soc Lond B Biol Sci* 345: 281–287.
- Thompson SC (1974) The colony forming efficiency of single cells and cell aggregates from a spontaneous mouse mammary tumour using the long culture assay. *Br J Cancer* 30: 332–336.
- Rafiqul FK, Tomkins SH, Madhisen R, Graff RA, Hahor FF, et al. (2002) Pulmonary and lymph node metastases is associated with primary tumor interstitial fluid pressure in human melanoma xenografts. *Cancer Res* 62: 661–664.
- van Deuren GH, de Boer M, Mominkhof EM, Bult P, van der Wall E, et al. (2000) Non-sentinel lymph node metastases associated with isolated breast cancer in the sentinel node. *J Natl Cancer Inst* 100: 1574–1580.
- Hansen NM, Grdic B, Ye X, Turner RR, Brenner RJ, et al. (2009) Impact of micrometastases in the sentinel node of patients with invasive breast cancer. *J Clin Oncol* 27: 4679–4684.
- Uribearena-Amezaga R, Ortega J, Fuentes J, Raventos N, Parra P, et al. (2010) Prognostic value of lymph node micrometastases in patients with colorectal cancer in Dukes stages A and B (T1–T4, N0, M0). *Rev Esp Enferm Dig* 102: 176–186.
- de Boer M, van Deuren GH, van Dijk JA, Borm GF, van Dieen PJ, et al. (2009) Micrometastases or isolated tumor cells and outcome of breast cancer. *N Engl J Med* 361: 653–663.
- de Boer M, van Dijk JA, Bult P, Borm GF, Tjonn-Heljesen VG (2010) Breast cancer prognosis and occult lymph node metastases: isolated tumor cells, and micrometastases. *J Natl Cancer Inst* 102: 410–425.
- Chen SL, Horluc EM, Giuliano AE (2007) The prognostic significance of micrometastases in breast cancer: a SEER population-based analysis. *Ann Surg Oncol* 14: 3378–3384.
- van den Brekel MW, Castelijns JA, Snow GB (1998) The size of lymph nodes in the neck on sonograms as a radiologic criterion for metastatic: how reliable is it? *AJNR Am J Neuroradiol* 19: 695–700.
- Castelijns JA, van den Brekel MW (2001) Detection of lymph node metastases in the neck: radiologic criteria. *AJNR Am J Neuroradiol* 22: 3–4.
- Williams AD, Cousins G, Soutter WP, Mubasher M, Peters AM, et al. (2001) Detection of pelvic lymph node metastases in gynecologic malignancy: a comparison of CT, MR, imaging, and positron emission tomography. *AJR Am J Roentgenol* 177: 343–349.
- Folkman J (1990) What is the evidence that tumors are angiogenesis dependent? *J Natl Cancer Inst* 82: 4–6.
- Ponn RT, Ng IO, Lau C, Yu WC, Yang ZF, et al. (2002) Tumor microvessel density as a predictor of recurrence after resection of hepatocellular carcinoma: a pilot retrospective study. *J Clin Oncol* 20: 1775–1785.
- Hanahan D, Folkman J (1996) Patterns and emerging mechanisms of the angiogenic switch during tumorigenesis. *Cel* 86: 353–364.
- Folkman J (1972) Anti-angiogenesis: new concept for therapy of solid tumors. *Ann Surg* 175: 409–416.

51. Toker C (1963) Some observations on the deposition of metastatic carcinoma within cervical lymph nodes. *Cancer* 16: 364–374.
52. Vakoc RJ, Fukumura D, Jain RK, Bouma BE (2012) Cancer imaging by optical coherence tomography: preclinical progress and clinical potential. *Nat Rev Cancer* 12: 363–368.

RESEARCH ARTICLE

Open Access

A novel autoantibody against fibronectin leucine-rich transmembrane protein 2 expressed on the endothelial cell surface identified by retroviral vector system in systemic lupus erythematosus

Tsuyoshi Shirai¹, Hiroshi Fujii^{1*}, Masao Ono², Kyohei Nakamura¹, Ryu Watanabe¹, Yumi Tajima¹, Naruhiko Takasawa¹, Tomonori Ishii¹ and Hideo Harigae¹

Abstract

Introduction: Anti-endothelial cell antibodies (AECAs) are thought to be critical for vasculitides in collagen diseases, but most were directed against molecules localized within the cell and not expressed on the cell surface. To clarify the pathogenic roles of AECAs, we constructed a retroviral vector system for identification of autoantigens expressed on the endothelial cell surface.

Methods: AECA activity in sera from patients with collagen diseases was measured with flow cytometry by using human umbilical vein endothelial cells (HUVECs). A cDNA library of HUVECs was retrovirally transfected into a rat myeloma cell line, from which AECA-positive clones were sorted with flow cytometry. cDNA of the cells was analyzed to identify an autoantigen, and then the clinical characteristics and the functional significance of the autoantibody were evaluated.

Results: Two distinct AECA-positive clones were isolated by using serum immunoglobulin G (IgG) from a patient with systemic lupus erythematosus (SLE). Both clones were identical to cDNA of fibronectin leucine-rich transmembrane protein 2 (FLRT2). HUVECs expressed FLRT2 and the prototype AECA IgG bound specifically to FLRT2-transfected cells. Anti-FLRT2 antibody activity accounted for 21.4% of AECAs in SLE. Furthermore, anti-FLRT2 antibody induced complement-dependent cytotoxicity against FLRT2-expressing cells.

Conclusions: We identified the membrane protein FLRT2 as a novel autoantigen of AECAs in SLE patients by using the retroviral vector system. Anti-FLRT2 antibody has the potential to induce direct endothelial cell cytotoxicity in about 10% of SLE patients and could be a novel molecular target for intervention. Identification of such a cell-surface target for AECAs may reveal a comprehensive mechanism of vascular injury in collagen diseases.

Introduction

Vascular endothelial cells (ECs) represent the boundary between blood and tissue, and contribute to the process of inflammation. Anti-endothelial cell antibodies (AECAs) were first described in 1971 and defined as autoantibodies that target antigens present on the EC membrane [1,2]. AECAs have been detected in a number of patients with collagen diseases, including systemic

lupus erythematosus (SLE), and were shown to be correlated to disease activity [3,4]. SLE is one of the diseases in which AECAs are frequently detected, and they are considered to play a role in the pathogenesis, especially in lupus nephritis [3,4]. In addition, SLE patients have an increased risk of cardiovascular disease originating from SLE itself, and it has been reported that AECAs play roles in atherosclerotic events [5].

AECAs have the potential to induce vascular lesions directly because their targets are expressed on ECs, which are always in contact with these circulating antibodies. AECAs are considered to play roles in the

development of pathologic lesions by EC cytotoxicity (complement-dependent cytotoxicity (CDC) and antibody-dependent cell-mediated cytotoxicity (ADCC)), activation of EC (proinflammatory cytokine secretion and expression of adhesion molecules), induction of coagulation, and induction of apoptosis [6-9].

Although new biologic drugs have been applied to the treatment of SLE, currently available therapies often introduce the additional risk of immunosuppression [10]. Bloom *et al.* [11] proposed a model for customized and specific therapeutic approaches against a highly pathogenic subset of lupus antibodies by using small molecules that neutralize them. AECAs may be good targets for such interventions, and identification of cell-surface targets of AECAs is required.

Target antigens of AECAs had been investigated intensively, but they are heterogeneous and classified into the following three groups: membrane component, ligand-receptor complex, and molecule adhering to the plasma membrane [12]. The cellular localization of the target antigen is considered to be a critical factor in the pathogenesis of autoantibodies [13], and it is generally accepted that autoantibodies against integral membrane proteins are usually pathogenic [14]. Although AECAs must be directed against the cell surface, most of the molecules reported to date as targets for AECAs are intracellular proteins [2,4,6,15]. Several groups have recently identified targets of AECAs by proteomics analysis [16,17]. However, extraction of some membrane proteins is difficult in proteomics analysis, and this may be one of the reasons that such proteins were not identified as AECA targets [2].

We constructed a retroviral vector system [18] to identify autoantigens expressed on the EC surface by using flow cytometry and identified the membrane protein fibronectin leucine-rich transmembrane protein 2 (FLRT2) as a novel autoantigen of AECAs in patients with SLE.

Materials and methods

Sources of human sera

Two hundred thirty-three patients with collagen diseases (196 female and 37 male patients) were enrolled in the study. The mean age was 42.5 years, with a range of 18 to 72 years. The patients comprised 95 with SLE and 138 with other collagen diseases. All of the patients were diagnosed according to the respective classification criteria [19-32]. Thirty-five age- and sex-matched healthy donors were enrolled as a control group. Sera were collected and stored at -20°C until use. All subjects gave written consent after the purpose and potential risks involved in the study were explained. The study protocol complied with the principles of the Declaration of Helsinki and was approved by the Ethical Committee of Tohoku University Graduate School of Medicine.

Cell culture

Human umbilical vein endothelial cells (HUVECs), human aortic endothelial cells (HAECs), human lung microvascular endothelial cells (HMVEC-Ls), and EGM-2 medium were purchased from Lonza (Basel, Switzerland). Human renal glomerular endothelial cells (HRGECs) and endothelial cell medium were purchased from ScienCell Research Laboratories (Carlsbad, CA, USA). The cells were grown in 5% CO₂ at 37°C on polystyrene flasks (BD Biosciences, Bedford, MA, USA). These ECs were used at sooner than the fifth passage. HEK293T cells were purchased from American Type Culture Collection (ATCC) (Manassas, VA, USA), Plat-E and Plat-GP packaging cells were purchased from Cell Biolabs (San Diego, CA, USA) and cultured in Dulbecco modified Eagle medium (DMEM) (Sigma, St. Louis, MO, USA) supplemented with 10% fetal bovine serum (FBS) (HyClone, Logan, UT, USA). Rat myeloma cells, YB2/0, were purchased from ATCC and cultured in RPMI1640 medium (Sigma) containing 10% FBS.

IgG purification

IgG fractions were purified from sera by using HITRAP Protein G HP columns (Amersham Biosciences, Rosendaal, The Netherlands). The concentration of purified IgG was determined by measuring the OD at 280 nm (OD₂₈₀). Purified IgG was stored at -20°C until use.

Flow cytometry

Binding activities of antibodies to the surface of ECs and FLRT2 molecules were measured by using FACSCalibur and FACSCanto II (Becton Dickinson, Franklin Lakes, NJ, USA) [17], and the data were analyzed with FlowJo Software (Tree Star, Ashland, OR, USA). In brief, attached cells were dissociated from plates by using Cell Dissociation Solution (Sigma) and washed with phosphate-buffered saline (PBS). Aliquots of 1 × 10⁵ cells/tube were incubated in blocking buffer (PBS containing 1% bovine serum albumin and 50 mg/ml goat gamma globulin fraction (Sigma)) with primary antibodies at 4°C for 30 minutes. After washing, cells were incubated with secondary antibodies and 7-amino-actinomycin D (7-AAD) (BD Biosciences) at 4°C for 30 minutes and analyzed with flow cytometry.

Primary antibodies included 1:10 diluted human serum, 0.5 mg/ml of purified human IgG, and 10 µg/ml goat anti-human FLRT1/FLRT2/FLRT3 antibody (R&D Systems, Minneapolis, MN, USA). Secondary antibodies included 1:50 diluted fluorescein isothiocyanate (FITC) or phycoerythrin (PE)-conjugated goat anti-human IgG (Abcam, Cambridge, UK), PE-conjugated donkey anti-goat IgG (Abcam), PE-conjugated mouse anti-human IgG1/IgG2/IgG3/IgG4 antibody (Beckman Coulter, Fullerton, CA, USA), and DyLight 650-conjugated anti human IgM antibody (Abcam). For staining of the intracellular FLRT2

* Correspondence: hfujii@med.tohoku.ac.jp

¹Department of Hematology and Rheumatology, Tohoku University Graduate School of Medicine, 1-1 Seiryō-cho, Aoba-ku, Sendai, Miyagi 980-8574, Japan
Full list of author information is available at the end of the article



domain, IntraStain (Dako, Glostrup, Denmark) and anti-human FLRT2 antibody (K-20) (Santa Cruz Biotechnology, Santa Cruz, CA, USA) were used.

For measurement of AECA activity, the relative mean fluorescence intensity (MFI) ratio was calculated as follows: (sample MFI - control MFI)/control MFI \times 100 [33]. Relative MFI ratio of mean \pm 3 standard deviations (SD) among the control group was defined as the cutoff value for AECAs. For measurement of anti-FLRT2 activity against the cell-surface domain, the relative MFI ratio was calculated as follows: (MFI against FLRT2-expressing cells - MFI against non-FLRT2-expressing cells)/MFI against non-FLRT2-expressing cells \times 100. In each set of experiments, relative MFI ratios of titrated reference serum with high anti-FLRT2 activity were calculated, and a standard curve was generated. The relative MFI ratio was converted to arbitrary units (AUs) according to the standard curve. AU of mean \pm 3 SD in the control group was defined as the cutoff value for the anti-FLRT2 antibody. Recombinant human FLRT2 (R&D Systems) was added at the indicated dose in inhibition tests. The percentage inhibition was calculated as follows: % inhibition = (AECA titer of sample serum - AECA titer of sample serum with inhibitor)/AECA titer of sample serum \times 100.

HUVEC cDNA library

Total RNA was generated from HUVECs by using an RNeasy Mini Kit (Qiagen, Hilden, Germany), and poly(A)⁺ RNA was purified with an mRNA Purification Kit (GE Healthcare, Little Chalfont, Buckinghamshire, UK). Double-stranded cDNA was synthesized by using a cDNA library construction kit (Takara Bio, Shiga, Japan). DNA fragments > 1,000 bp in length were ligated into the pMX vector (kindly donated by Toshio Kitamura, University of Tokyo, Tokyo, Japan).

Screening of cDNA library

The HUVEC cDNA library in pMX was retrovirally transfected into the YB2/0 rat myeloma cell line [34]. Aliquots of 1×10^7 YB2/0 cells expressing the HUVEC cDNA library were incubated with 0.5 mg/ml of IgG with high AECA activity at 4°C for 30 minutes. After washing, cells were incubated with FITC-conjugated goat anti-human IgG and 7-AAD at 4°C for 30 minutes. The cells showing a high level of FITC fluorescence signal were sorted with FACS Vantage (Becton Dickinson). Sorted cells were kept in culture until the cell number increased sufficiently for the next round of sorting. Subcloning of cells bound to IgG with AECA activity was performed by the limiting dilution method.

Genomic DNAs of clones were purified by using the Wizard SV Genomic DNA Purification system (Promega Corporation, Madison, WI, USA). DNA fragments from the HUVEC cDNA library were amplified by polymerase

chain reaction (PCR) by using TaKaRa LA Taq (Takara Bio) with primers corresponding to the 5' and 3' ends of the multiple cloning site of pMX (5'-GGTGGAC-CATCCTCTAGACTG, 3'-CCTTTTCTGGAGAC-TAAAT, respectively). The PCR products were cloned into the pCR-TOPO vector (Invitrogen), and DNA sequences were analyzed with the BLAST program.

Expression of FLRT2 in HEK293T cells

The full-length FLRT2 fragment was amplified by PCR from genomic DNA of FLRT2-expressing YB2/0 clone sorted as described earlier, by using Phusion High-Fidelity DNA Polymerase (Finnzymes, Keilaranta, Espoo, Finland). Primer sequences were as follows: 5'-CCCACCATTG-TATTTTATTTC, 3'-CITGATAACGCTGGCCCTCT. The FLRT2 fragment was inserted into the pMX-IRES-GFP vector (Cell Biolabs). An FLRT2 expression vector with deletion of the unique region was made by using an In-Fusion HD Cloning Kit (Clontech Laboratories, Madison, WI, USA) with two PCR segments constructed to omit the unique region (363 to 419 amino acids) and inserted into the pMX-IRES-GFP vector. pMX-FLRT2-IRES-GFP was transfected directly into HEK293T cells with FuGENE HD (Roche Diagnostics, Basel, Switzerland) or retrovirally transfected into HEK293T cells. Full-length FLRT1 and FLRT3 fragments were amplified as described earlier and inserted into the pMX-IRES-GFP vector.

Western blotting

Cells were lysed in RIPA buffer (Cell Signaling Technology, Danvers, MA, USA). The lysate was mixed with 5 \times sodium dodecyl sulfate (SDS) sample buffer and separated by electrophoresis on an 8% polyacrylamide gel. The proteins were then transferred onto Immobilon Transfer Membranes (Millipore, Billerica, MA, USA). The membranes were treated with 0.1 μ g/ml of goat anti-FLRT2 antibody and IRDye680-conjugated donkey anti-goat IgG (LI-COR Biosciences, Lincoln, NE, USA), and fluorescence intensity was determined with the Odyssey infrared imaging System (LI-COR).

CDC

CDC was assessed by the tetrazolium salt reduction method by using WST-1 (Roche Diagnostics) [35-37]. In brief, cells were seeded in 96-well culture plates at a concentration of 4×10^4 cells per well and cultured overnight. Cells were incubated with 100 μ l of diluted IgG for 30 minutes followed by addition of 50 μ l of rabbit complement (Cedarlane Laboratories, Burlington, ON, Canada) at the indicated concentrations for 2 hours at 37°C. Then 15 μ l of WST-1 was added, and cells were incubated for an additional 4 hours. Absorbance at 450 nm (A_{450}) was measured and expressed as relative fluorescence units (RFUs), reflecting the number of viable cells. Triton X-100 (1%)

and heat-inactivated complement were added to the wells to measure background or maximal absorbance of WST-1, respectively. Recombinant FLRT2 was added in the inhibition tests. The percentage cytotoxicity for each sample was calculated by using the formula:

$$\% \text{ cytotoxicity} = (\text{maximal RFU} - \text{sample RFU}) / (\text{maximal RFU} - \text{background RFU}) \times 100.$$

ADCC

ADCC was determined by using the LDH Cytotoxicity Detection Kit (Takara Bio) and the manufacturer's protocol [36].

The percentage cytotoxicity was calculated as follows:

$$\% \text{ cytotoxicity} = (\text{experimental cell lysis} - \text{spontaneous cell lysis}) / (\text{target maximum} - \text{spontaneous cell lysis}) \times 100.$$

Detection of adhesion molecule expression

HUVECs were cultured overnight in 96-well culture plates and incubated with IgG (640 μ g/ml) for 6 hours at 37°C. Harvested cells were stained with PE-conjugated anti-CD62E antibody (BioLegend, San Diego, CA, USA), allophycocyanin (APC)-conjugated anti-CD106 antibody (BioLegend), and Pacific blue-conjugated anti-CD54 antibody (BioLegend), and were analyzed with flow cytometry.

Detection of EC apoptosis

HUVECs were seeded in 48-well culture plates and incubated with test IgG (640 μ g/ml) for 24 hours, and apoptosis in the harvested cells was measured with annexin V and 7-AAD (Apoptosis Detection Kit; BD Biosciences) with flow cytometry. Annexin V-positive/7-AAD-negative cells were measured as apoptotic cells.

Statistical analysis

Data were analyzed by using the two-tailed Student *t* test or Mann-Whitney *U* test for continuous variables. Pairwise comparisons were assessed by using the Wilcoxon signed-rank test. Spearman rank correlation was used to explore the associations between anti-FLRT2 titer and clinical parameters. All analyses were performed by using Prism software (GraphPad Software, La Jolla, CA, USA). In all analyses, *P* < 0.05 was taken to indicate statistical significance.

Results

Detection of AECA activity with flow cytometry

We first examined AECA activity in the sera from patients with collagen diseases by measuring binding activity of IgG to nonpermeabilized 7-AAD-negative HUVECs by using flow cytometry. The prevalence of AECAs was significantly higher in patients with SLE (50.5%) and other collagen diseases compared with normal controls (2.9%)

(Figure 1). As these data indicated the presence of autoantigens on the EC surface, we constructed a retroviral vector system to identify cell-surface target molecules of AECAs with flow cytometry.

Sorting of cells expressing cell-surface autoantigens with retroviral vector system

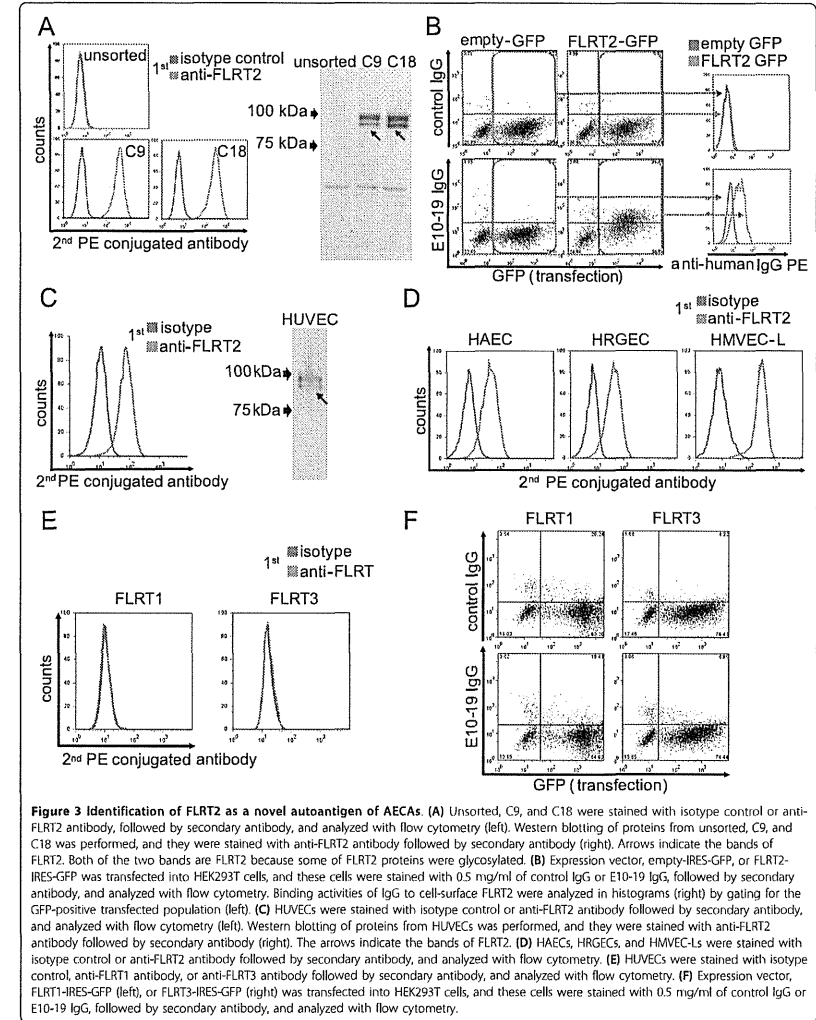
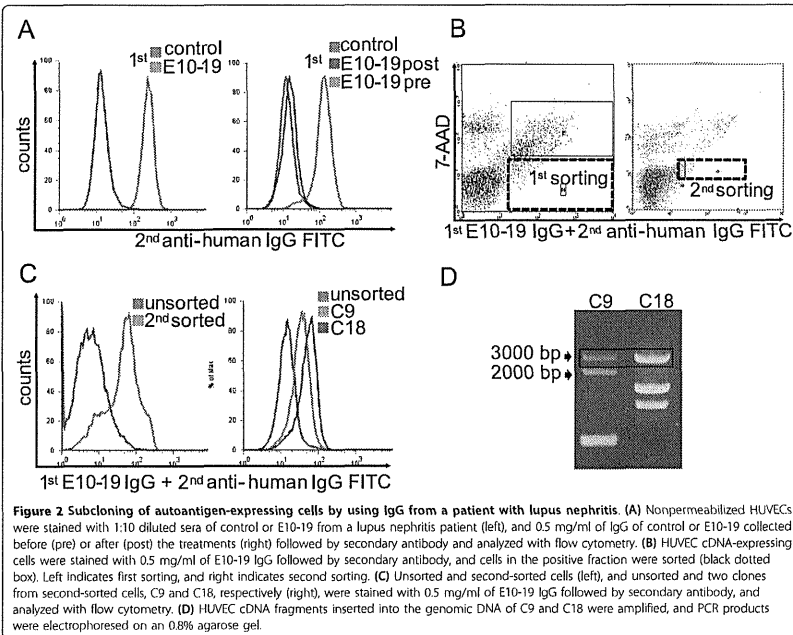
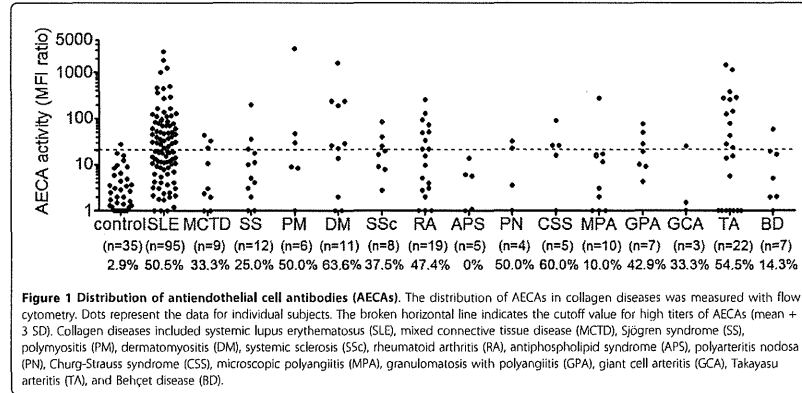
Among sera with AECA activity, one sample (E10-19) from an SLE patient with active lupus nephritis (WHO IV) showed strong AECA activity (Figure 2A). We selected this serum sample as the prototype of AECAs for subsequent cell sorting. Purified IgG from E10-19 serum also showed strong binding to the surface of HUVECs, and IgG from the same patient collected after the treatment with 1 mg/kg prednisolone and intravenous cyclophosphamide showed remarkably reduced AECA activity (Figure 2A).

The YB2/0 cell line expressing HUVEC cDNA was generated by stable transfection of the HUVEC cDNA library with the retroviral vector system. After staining of this cell line with E10-19 IgG and FITC-conjugated secondary antibody, cells with strong FITC signals were sorted with flow cytometry. After cell expansion, we repeated one more round of cell sorting to concentrate E10-19 IgG-binding cells (Figure 2B). After the second sorting, cells bound to E10-19 IgG were markedly increased, and several cell clones were established from the E10-19 IgG-binding cell population by the limiting dilution method. Two distinct clones with different E10-19 IgG-binding activities and gene profiles of transfected HUVEC cDNA were established, C9 and C18 (Figure 2C and 2D).

Identification of FLRT2 as a novel cell-surface autoantigen

After PCR amplification and cloning of HUVEC cDNA inserted into the genomic DNA of C9 and C18, DNA sequencing was performed followed by BLAST analysis. PCR bands of around 3,000 bp in C9 and C18 (Figure 2D, black box) were found to be an identical gene, that is, fibronectin leucine-rich transmembrane protein 2 (*FLRT2*) cDNA (GenBank accession number NM_013231.4). Real-time quantitative PCR and microarray analysis of YB2/0, C9, and C18 also supported the conclusion that only the *FLRT2* mRNA was overexpressed in both C9 and C18 (data not shown). Flow cytometry and Western blotting showed that FLRT2 protein was expressed on the cell surfaces of C9 and C18 (Figure 3A). Next, we generated an expression vector of FLRT2, which was transfected into HEK293T cells. E10-19 IgG showed significant binding activity to 7-AAD-negative FLRT2-expressing HEK293T cells (Figure 3B), indicating that E10-19 IgG has high anti-FLRT2 activity. Thus, the membrane protein FLRT2 was identified as a novel autoantigen.

Flow cytometry and Western blotting indicated that HUVECs and other ECs also expressed significant levels



of FLRT2 on their cell surfaces (Figure 3C, D). FLRT2 is a member of the FLRT family, which includes FLRT1, FLRT2, and FLRT3 [38]. We examined whether other FLRTs were expressed on HUVECs with flow cytometry. Neither FLRT1 nor FLRT3 was expressed on the surface of these ECs, and E10-19 IgG showed no binding activity to either FLRT1 or FLRT3 (Figure 3E, F). These data indicated that among the FLRT family, FLRT2 was the only target molecule of AECA.

Inhibition test and epitope mapping

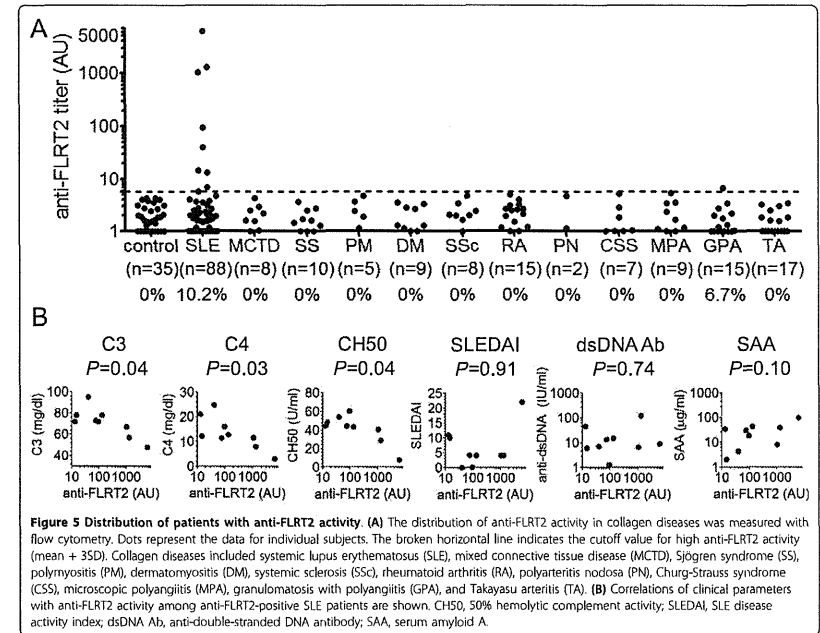
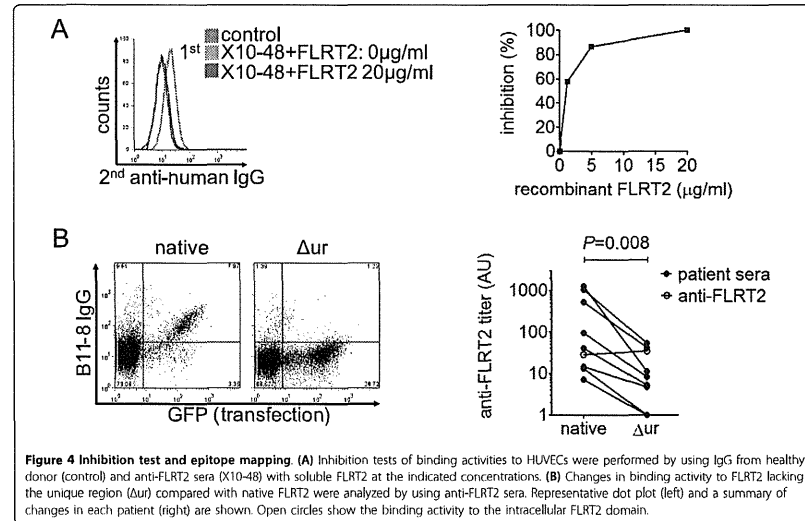
We conducted inhibition tests to determine whether the AECA activities of anti-FLRT2-positive SLE patients were due to anti-FLRT2 activity. Incubation with soluble recombinant FLRT2 inhibited the binding of patient IgG to HUVECs (Figure 4A). We further investigated the epitope of anti-FLRT2 antibody. FLRT2 contains extracellular leucine-rich repeats, unique region, fibronectin type III domain, and a cytoplasmic tail. As mentioned earlier, FLRT2 was the only member of the FLRT family that was bound by SLE IgG, so we hypothesized that the unique region of FLRT2 may be the major epitope for anti-FLRT2 antibody. To investigate this hypothesis, an expression vector of FLRT2 lacking the unique region (FLRT2 Δ ur) was generated. As shown in Figure 4B, the

binding activity of the anti-FLRT2 antibody was significantly reduced when FLRT2 lacked its unique region ($P = 0.008$) compared with the equal binding activity of anti-FLRT2 antibody to the intracellular domain. These observations indicated that the major epitope was localized within the unique region of FLRT2.

Distribution of patients with anti-FLRT2 activity

Anti-FLRT2 activities were detected in nine (10.2%) of 88 patients with SLE and one (6.7%) of 15 patients with granulomatosis with polyangiitis (Wegener's). Healthy controls and other patients with collagen diseases, including diseases that showed a high prevalence of AECA activity, did not show anti-FLRT2 activity (Figure 5A). Strong anti-FLRT2 activities were detected in only SLE patients, indicating that anti-FLRT2 antibody is specific to SLE patients. Among 48 SLE patients with AECA positivity (Figure 1), 42 were examined for anti-FLRT2 activity, and nine patients (21.4%) were positive.

Among SLE patients with anti-FLRT2 positivity, anti-FLRT2 activity was significantly correlated with low levels of complement C3, C4, and CH50 (Figure 5B). No interrelations were found between anti-FLRT2 activity and the SLE disease activity index (SLEDAI), anti-dsDNA antibody titer, or serum amyloid A (SAA) level (Figure 5B).



Induction of endothelial cell killing by CDC

We next assessed the functional significance of anti-FLRT2 antibody by using IgG from the sera of two SLE patients with high FLRT2 activity (B11-8 and X10-48). IgG with anti-FLRT2 activity showed significant CDC activity against HUVECs compared with IgG from normal controls (Figure 6A). This CDC activity was inhibited by incubation with soluble recombinant FLRT2, and increased with a higher concentration of IgG (Figure 6B, C). Strong CDC activity was induced against FLRT2-expressing HEK293T cells, but not against mock-transfected HEK293T cells (Figure 6D). These observations confirmed the ability of the anti-FLRT2 antibody to induce CDC activity by binding to cell-surface FLRT2.

We also analyzed the IgG subclasses of anti-FLRT2 antibody with flow cytometry. In all anti-FLRT2 active IgG subclasses, IgG1 and IgG2 activities were strong, and IgG3 was weak. The presence of IgG4 varied between patients (Figure 6E). Compared with IgG, weak

IgM activity was detected (Figure 6F). None of these IgGs showed ADCC (Figure 6G).

Other pathogenic roles as AECA

We examined further potentials for pathogenicity against EC activation and induction of apoptosis. The levels of expression of adhesion molecules (intercellular adhesion molecule 1 (ICAM-1), vascular cell adhesion molecule 1 (VCAM-1), and E-selectin) on HUVECs were not increased by incubation with IgG purified from B11-8 and X10-48 compared with control IgG (Figure 7A). Incubation of HUVECs with anti-FLRT2-positive IgG did not induce apoptosis (Figure 7B).

Discussion

Although the existence of AECA in patients with SLE and other collagen diseases has been reported, its pathogenic significance remains unknown. The localization of the AECA target molecule on the cell surface should be